Chapter 7

ULTIMATE BEARING CAPACITY OF STRIP FOUNDATION ON UNSATURATED SOIL BY UB-FELA TECHNIQUE

7.1 INTRODUCTION

In the previous chapters, axisymmetric stability problems are analyzed based on the assumption that the soil strata are either completely dry or saturated. However, in reality, a significant soil portion below the foundations remains in an unsaturated condition. The groundwater tables are located tens of meters below the surface in some semiarid to arid areas, implying that the shallow load-bearing soil layers may never become fully saturated. Moreover, the employment of drainage systems and hydraulic barriers beneath shallow foundations (Maghvan et al. 2019) further makes the environment conducive to the attainment of a variably saturation state. Also, the climatic conditions such as infiltration and evaporation directly or indirectly result in substantial and unprecedented changes in the degree of saturation within the unsaturated zone.

In the mid-half of the previous century, a few researchers (Meyerhof, 1951; Vesic, 1973) advocated the need to consider the matric suction (ψ) in the vadose zone; however, most of the work on the load-bearing estimation of shallow footings were carried out in the last three decades (Oloo, 1994; Costa et al., 2003; Mohamed and Vanapalli, 2006, 2012; Rojas et al., 2007; Oh and Vanapalli, 2008; Oh and Vanapalli, 2011; Vanapalli and Mohamed, 2013; Vo and Russell, 2016; Tang et al., 2017; Yan et al., 2020; Yuan and Du, 2020; Du et al., 2021; Roy and Chakraborty, 2023). By treating ψ as a constant apparent cohesion, Oloo (1994) and Costa et al. (2003) modified the

classical Terzaghi's bearing capacity formulations to predict the strength aspect of a partially saturated soil. Mohamed and Vanapalli (2006, 2012) performed an experimental test on sandy soil. They observed that the bearing capacity of unsaturated soil at 8 kPa ψ was almost 3.5 times that of saturated soil. In addition, the bearing capacity of soil increased nonlinearly in the presence of ψ. Several other experimental works (Rojas et al., 2007; Oh and Vanapalli, 2008, 2011, 2013) showed the nonlinear profile of ψ along the vertical height above the water table (y). Based on the nonlinear variation in ψ, a few analytical and numerical works (Vo and Russell, 2016; Tang et al., 2017; Yan et al., 2020; Yuan and Du, 2020; Du et al., 2021; Anand and Sarkar, 2022) were carried out to investigate the load-carrying behaviour of strip footings under various steady flow conditions. However, to the best of the authors' knowledge, the rigorous limiting value of the bearing capacity of footings was never investigated on unsaturated soils. This chapter presents the modifications carried out in the upper-bound formulations to compute the ultimate bearing capacity of plane-strain footings. Strip foundations are undoubtedly ubiquitous plane-strain structures in geotechnical engineering as they are widely used in buildings, retaining walls, and many other long structures. The upper bound limit technique is executed with finite elements and linear optimization. The aspect of the variable degree of saturation is incorporated using the unified effective stress (σ') concept that was proposed by Lu and Likos (2004). The soil suction characteristics curve is formed by combining all the aspects of USM as described in Chapter 1. The hydromechanical properties, SWRC model parameters, soil strength parameters, and location of the groundwater table are widely varied, and the corresponding bearing capacity factors are evaluated with and without surcharge. In addition, the nodal velocity patterns are drawn for a few cases.

The chapter comprises three different sections- (i) the first section elaborates on the concept of unsaturated mechanics, (ii) the second part illustrates the formulation of upper bound solution incorporating suction stress by using linear optimization, and (iii) the third segment presents the numerical upper bound bearing capacity of a strip footing resting on unsaturated soil.

7.2 Construction of SSCC curves

By employing Gardner's HCF model, steady-state flow rate, *q*, and the boundary condition of zero suction at the groundwater table (y = 0), the expression of matric suction is obtained by integrating Equation (1.3) within the integration limit of 0 to y.

$$(u_a - u_w) = -\frac{1}{\alpha}\ln\left[\left(1+\frac{q}{k_s}\right)e^{-\gamma_w \alpha y} - \frac{q}{k_s}\right] \tag{7.1}$$

For no-flow condition (i.e., q =0), matric suction boils down to: $(u_a - u_w) = y\gamma_w$. And, therefore, the linear distribution of the hydrostatic stress in the vadose zone.

By substituting the expression of matric suction and S_e in Equation (1.6b), the explicit form of σ^s can be mathematically rewritten as:

$$\sigma^s = -(u_a - u_w)S_e = -\frac{(u_a - u_w)}{\left\{1+\left[\alpha(u_a - u_w)\right]^n\right\}^m} = \frac{1}{\alpha}\frac{\ln\left[\left(1+\frac{q}{k_s}\right)e^{-\gamma_w \alpha y} - \frac{q}{k_s}\right]}{\left(1+\left\{-\ln\left[\left(1+\frac{q}{k_s}\right)e^{-\gamma_w \alpha y} - \frac{q}{k_s}\right]\right\}^n\right)^m} \tag{7.2}$$

Here, α, n, and m are the unsaturated soil property functions of the vadose zone. This closed-form equation is generated from the vG-SWRC model, Gardner's one-parameter HCF model, Darcy's flow law, and continuity equation and is a function of unsaturated property functions, flow ratio, and fluid density. This relation is valid for all types of soils and is known as the *soil suction characteristics curve*.

It is to be noted that SSCC and SWRC are intrinsically related (Nuth and Laloui, 2008; Zhou et al., 2012), and therefore, the hydromechanical and flow parameters considered in both expressions are the same. A number of researches clearly (Pham et al., 2005; Gallage et al., 2013; Gao et al., 2019; Kido et al., 2020; Ma et al., 2020; Wen et al,. 2020) show that the water retention curves show significant hysteretic behaviour. Moreover, the SWRC and the HCF curves depend highly on the net normal stress and initial density (Ng and Pang, 2000; Gallipoli et al., 2003; Sun et al., 2007; Masin, 2010; Sheng and Zhou, 2011). However, in the present study, the effects of state parameters on the development of the suction are not taken into consideration. Recently, Patil et al. (2020) conducted a series of experiments on cohesive–frictional soils for a wide range of suctions by employing suction-controlled true triaxial, ring shear, and plane strain (biaxial) tests apparatus. These tests established the validity and practical applicability of the SSCC model.

7.3 Impact of the model parameters on SWRC, HCF, and SSCC models

7.3.1 van -Genuchten's SWRC model

Figure 7.1 shows the impact of the fitting parameters on the SWRC curves. Increasing α results in a decrease in the air entry value; nevertheless, the SWRC curves in the transition zone are parallel. Figure 7.1b shows that desaturation commences at the same matric suction for the same α, but the desaturation rate gets highly influenced by the *n* value. The higher the *n* faster is the process of desaturation. It is to be noted that SWRC curves also indicate the pore-size geometry and distribution within the considered soil. Lower *n* indicates well-gradation, whereas uniformly (poorly) graded soil is characterized by a high value of *n*. However, the shape of the SWRC curve adjacent to the residual state is wholly controlled by the *m*-parameter. In a sense, *m*

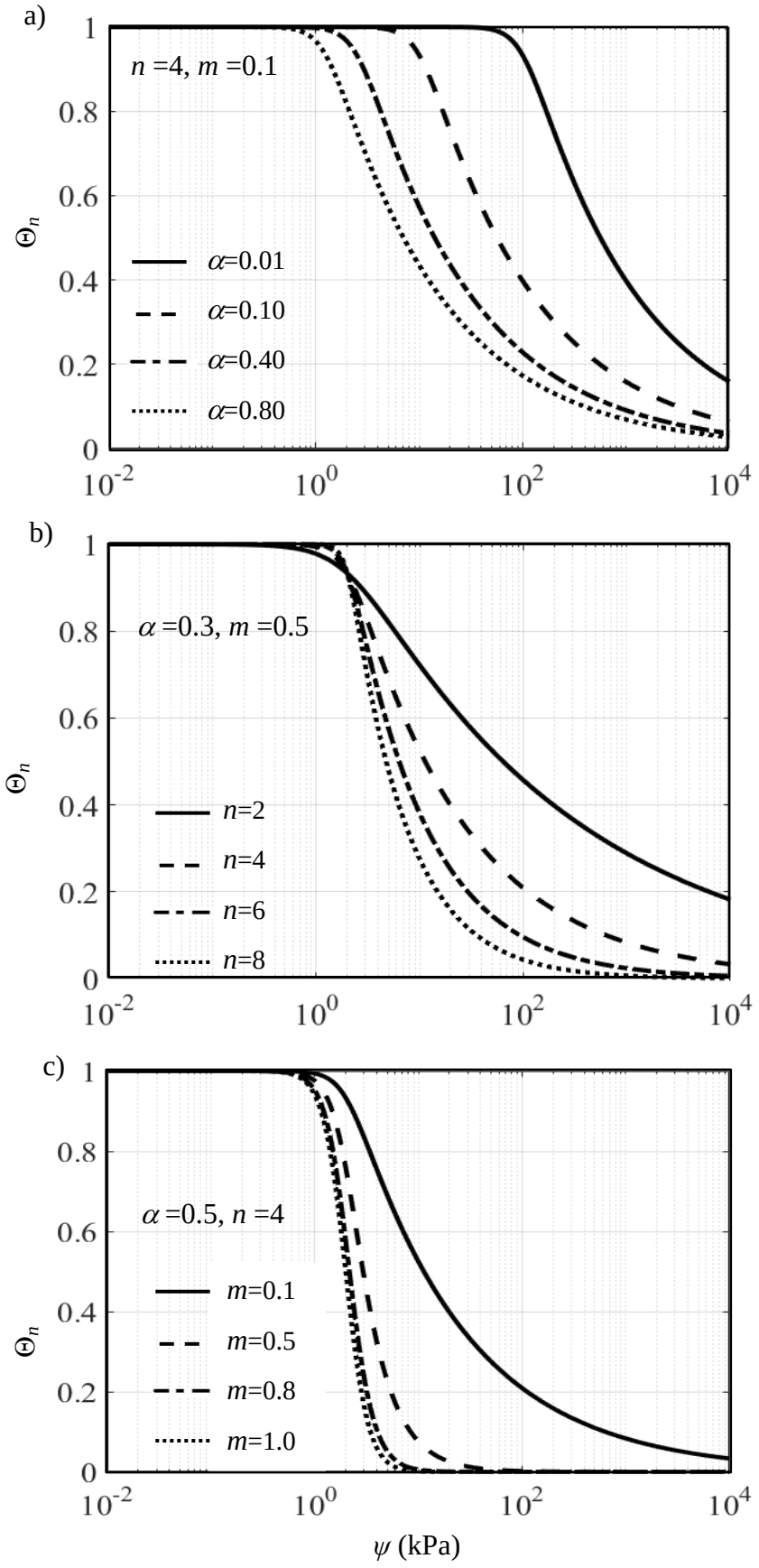

Figure 7.1 The variation of normalized water content with matric suction for different value of: a) α (=0.01, 0.10,0.40,0.80); b) n (=2,4,6,8); c) m (=0.1, 0.5,0.8,1).

governs the asymmetricity of the SWRC curve by providing greater flexibility in fitting SWRC data. For obtaining a closed-form solution, following Mualem's (1976) permeability model, m is assumed to bear the following fixed relationship with n: m=1−1/n. To encompass the wide variability of m, various K_M parameters (K_M =m −1+1/ n), which relate m with n, are chosen in the present chapter.

7.3.2 Gardner's HCF model

Figure 7.2 displays the variation of k, in a log-log graph, for (a) two clayey soils (with k_s =1x10^{-8} m/s) having α =0.001 and α =0.003, and (b) two sandy soils (with k_s =1x10^{-5} m/s) having α =0.1 and α =0.3. For sandy soils, the permeability starts to drop at low matric suction and at a significantly faster rate. A striking feature of unsaturated

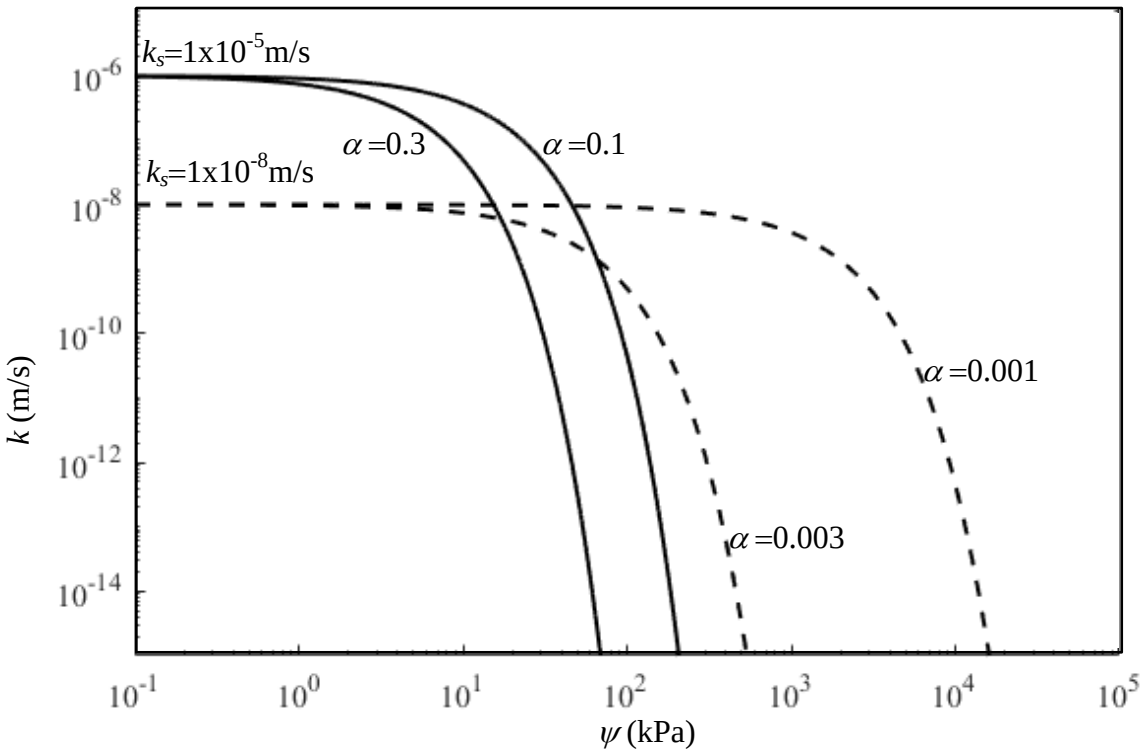

Figure 7.2 The variation of k, for clayey soils (k_s =1x10^{-8} m/s) having α =0.001 and α =0.003, and sandy soils (k_s =1x10^{-5} m/s) having α =0.1 and α =0.3.

soil mechanics becomes evident in this pattern: once a certain matric suction is exceeded, the permeability of sand drastically decreases compared to that of clay.

7.3.3 Lu and Likos's SSCC model

Figure 7.3 illustrates the variation of σ^s with respect to y pertaining to various combinations of n, α and m; Figures 7.3a, 7.3b, 7.3c are associated with K_M =0, whereas Figures 7.3d and 7.3e correspond to K_M =2, and K_M =4, respectively. It is noticed that upto a certain height above the water table, σ^s rises at a significant rate, and thereafter, either it attains a constant plateau or it starts decreasing and asymptotes towards the zero-suction line. For uniformly-graded soils, maximum suction stress increases, peak point becomes sharper, and the asymptotic trend starts earlier. For a certain n value, the suction stress profiles significantly fall as the magnitude of α decreases from 0.1 to 0.3. Regardless of the flow conditions, the generated suction stress profiles are unique for the chosen range of α. There is a further variation of the suction stress profile as K_M is taken differently; Figures 7.3b, 7.3d, and 7.3e present the suction stress profiles for K_M equal to 0, 2, and 4, respectively. The band gap, where the suction stress remains non-zero, decreases nonlinearly as K_M increases.

7.4 UPPER BOUND FINITE ELEMENT LIMIT ANALYSIS FORMULATION

In order to obtain the upper bound collapse load, a kinematically admissible velocity field is required to be constructed over the considered soil domain. For ensuring kinematical admissibility, the velocity and the strain field must satisfy the: i) strain-displacement relation, ii) normality rule of plastic flow, and iii) velocity boundary conditions. By virtue of limit theorems, the soil is considered to be perfectly plastic material and following an associated flow rule. The domain is discretized with three nodded linear (constant-strain) triangular elements. Each node is associated with two degrees of freedom (unknown velocity variables), namely, horizontal velocity (u) and vertical velocity (v), Figure 7.4 shows a typical element alongwith the ascribed nodal

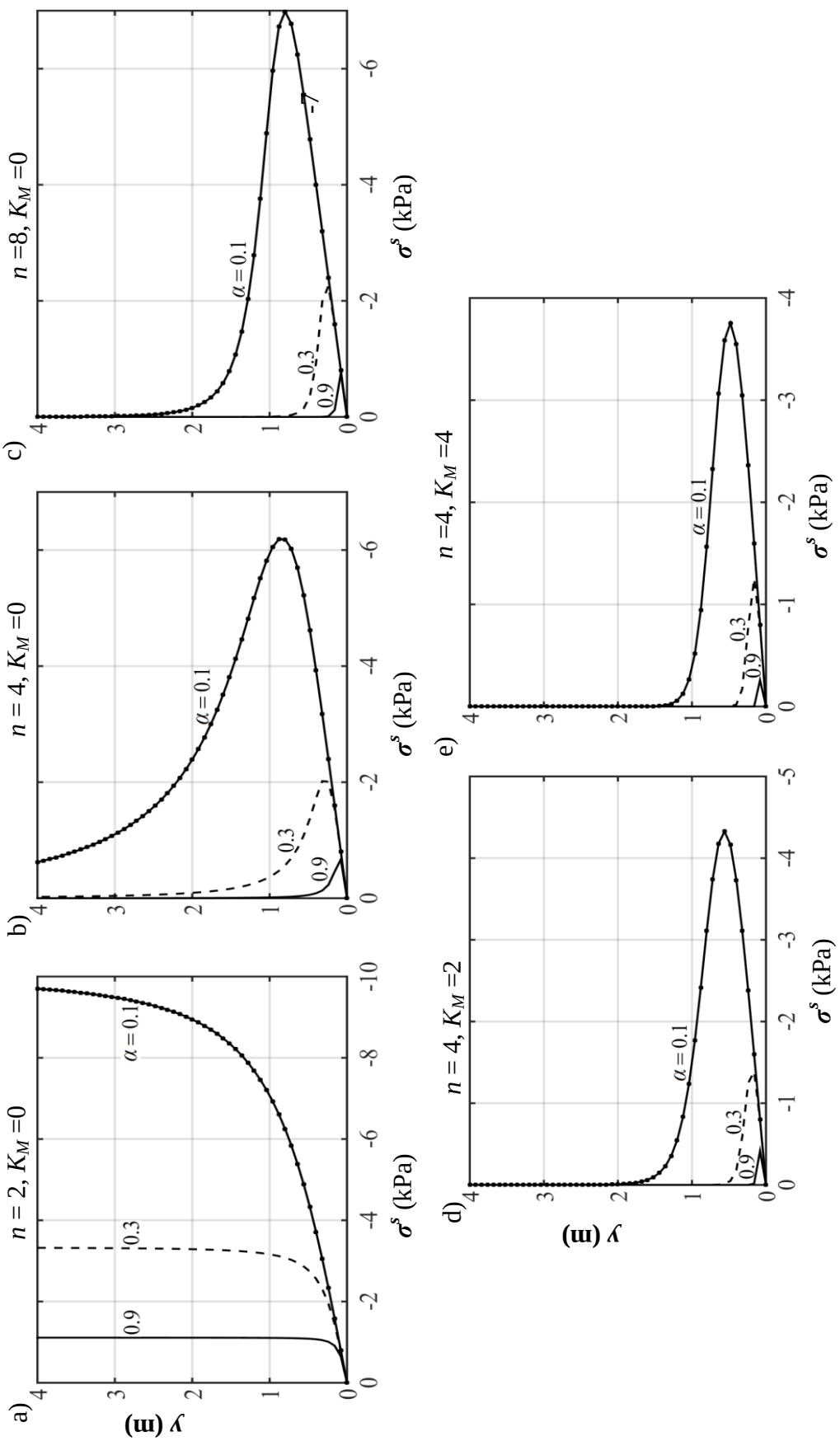

Figure 7.3 The variation of σ^s with depth above water table for different value of α (0.1, 0.3, 0.9) that corresponded to (a) n=2 and K_M=0; (b) n =4 and K_M=0; (c) n =8 and K_M =0; (d) n =2 and K_M =2; and (e) n =2 and K_M =4.

velocities. Within a given element *e*, the velocities are assumed to vary linearly by using the following expressions:

$$u = \sum_{i=1}^{3} N_i u_i \quad ; \quad v = \sum_{i=1}^{3} N_i v_i \tag{7.3}$$

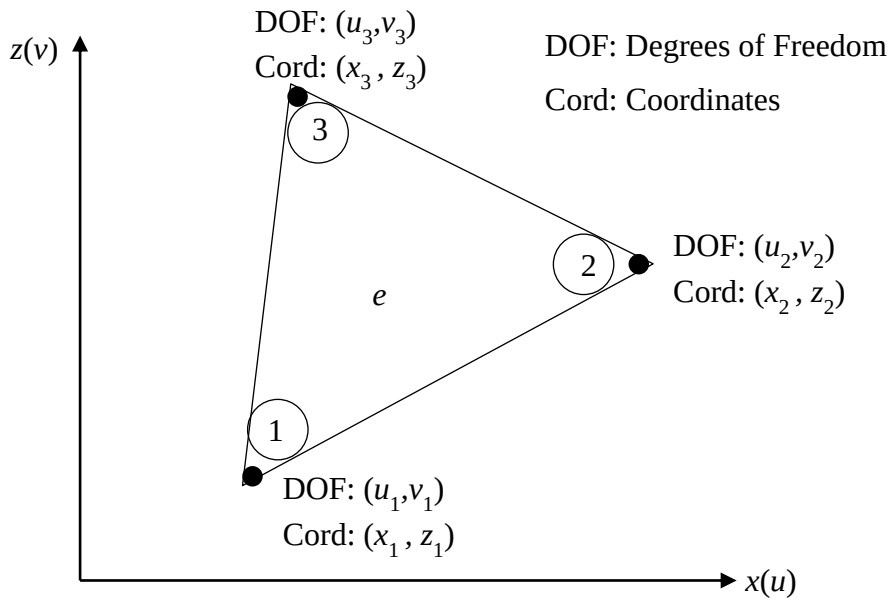

Figure 7.4 A typical triangular element for performing an upper bound limit analysis

where, u_i and v_i are the velocities at i^{th} node and N_i is the linear shape function defined as:

$$N_i = \frac{1}{2A^e}\left[(x_j z_k - x_k z_j) + z_{jk} x + x_{kj} z\right] \tag{7.4}$$

where, (a) *i*, *j* and *k* are the three nodes (numbered in a counter-clockwise direction) of a triangular element in a *x*–*z* plane, (b) x_{jk} (difference in *x* coordinates) = $x_j - x_k$; z_{jk} (difference in *z* coordinates) = $z_j - z_k$, and (c) A^e (area of the element) = $0.5 \left| x_{ik} z_{jk} - x_{kj} z_{ki} \right|$.

The upper bound formulations for the unsaturated soil remain almost similar to that of saturated soil, except few modifications that are required to be adapted due to the

change in the form of the yield function. Unlike, the saturated soil mechanics, the size of MC yield circle (Figure 7.5a) or, in other words, the position of the MC failure envelope (Figure 7.5b) corresponds to the variably saturated soil does not remain to be

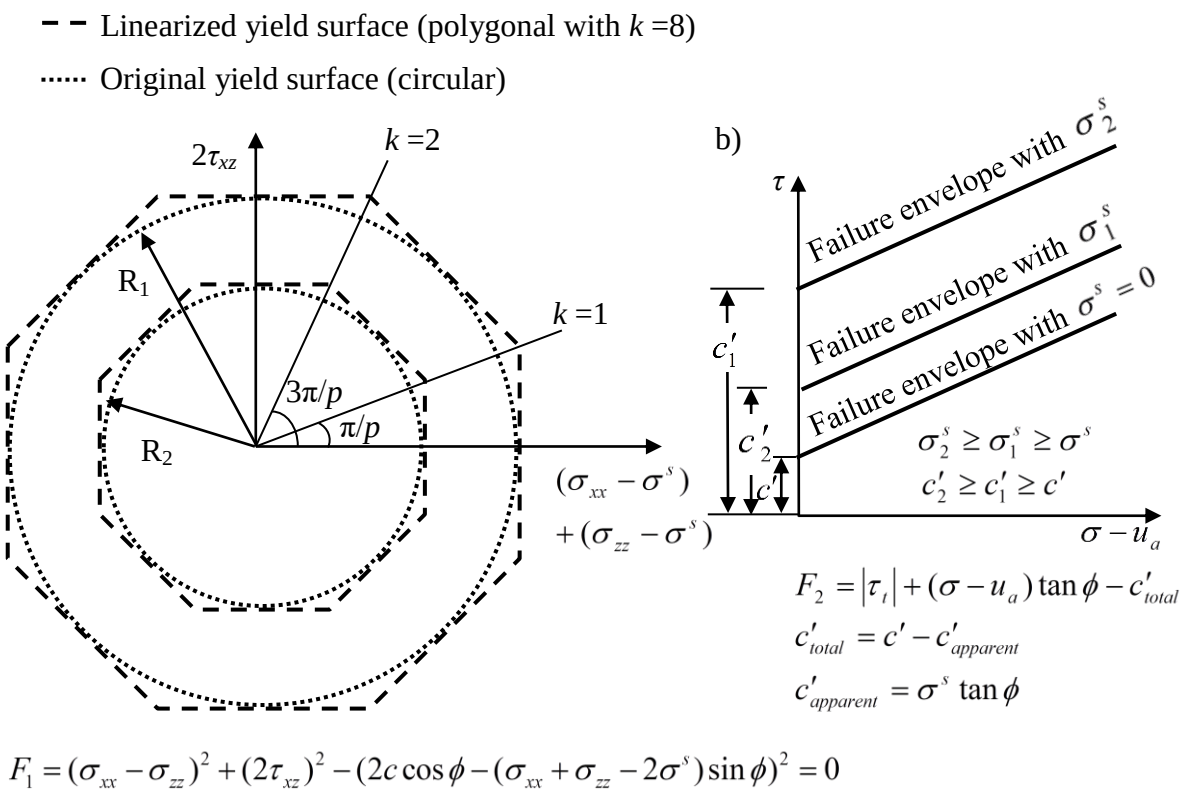

$$F_1 = (\sigma_{xx} - \sigma_{zz})^2 + (2\tau_{xz})^2 - (2c\cos\phi - (\sigma_{xx} + \sigma_{zz} - 2\sigma^s)\sin\phi)^2 = 0$$

Figure 7.5 a) Modified MC yield surface and its linearization; and b) modified MC yield envelope.

constant; rather it changes with the suction stress which is again a function of spatial coordinate. Therefore, the components of the objective function and the constraints that evolve with the employment of the yield function requires reconstruction so that the impact of suction stress in the variably saturated soil gets duly incorporated. The imposed constraints and the objective function are detailed below.

7.4.1 Constraints within the elements arising from the plastic flow

To derive the constraint within the continuum element, the strain–displacement relation and the associative flow rule (AFR) are employed. The strain–displacement

relation and the AFR connect the plastic strain rates with the gradient of the velocity components, and the yield function, as shown below:

$$\dot{\varepsilon}_{ij} = \frac{1}{2}\left(\frac{\partial u_i}{\partial x_j} + \frac{\partial u_j}{\partial x_i}\right) = \dot{\lambda}\frac{\partial F_1}{\partial \sigma_{ij}} \tag{7.5}$$

where, (i) $\dot{\varepsilon}_{ij}$ and σ_{ij} =plastic normal strain rate and the stress components, respectively, which are associated with each node for the plane strain condition; (ii) u_i and v_i = unknown velocities at i^{th} node. $\dot{\lambda}$ is a non-negative plastic multiplier rate, and (iii) F_1= form of the modified MC yield circle, which is constructed based on the σ^s–based σ' formulation. Using Equation (7.2), the extended MC yield circle can be expressed as:

$$F_1 = (\sigma_{xx} - \sigma_{zz})^2 + (2\tau_{xz})^2 - (2c\cos\phi - (\sigma_{xx} + \sigma_{zz} - 2\sigma^s)\sin\phi)^2 = 0 \tag{7.6}$$

It is to be noted that for the sake of convenience, the pore air pressure is set to the reference atmospheric pressure, i.e., u_a equals to zero. In order to avoid the computational complexities of the nonlinear nature of F_1, following Sloan and Kleeman (1995), the MC yield circle is linearized by considering an external polygon with p number of sides, as shown in Figure 7.5a. Each of the straight lines can be expressed as the following:

$$F_{1k} = A_k\sigma_{xx} + B_k\sigma_{zz} + C_k\tau_{xz} - 2(c\cos\phi - \sigma^s\sin\phi) = 0 \tag{7.7}$$

where, A_k = cos (2πk/p) + sinϕ ; B_k= sinϕ – cos (2πk/p) ; C_k= 2 sin (2πk/p) ; k = 1, 2,. ,p. Unifying Equations (7.5) and (7.7), the relation between the velocity variables and the plastic multipliers can be expressed as below:

$$\dot{\varepsilon}_{xx} = \frac{\partial u}{\partial x} = \sum_{i=1}^{3} u_i\frac{\partial N_i}{\partial x} = \sum_{k=1}^{p}\dot{\lambda}_k\frac{\partial F_{1k}}{\partial \sigma_{xx}} \quad \Rightarrow \quad \sum_{i=1}^{3} u_i\eta_i = \sum_{k=1}^{p}\dot{\lambda}_k A_k \tag{7.8a}$$

$$\dot{\varepsilon}_{zz} = \frac{\partial v}{\partial z} = \sum_{i=1}^{3} v_i\frac{\partial N_i}{\partial z} = \sum_{k=1}^{p}\dot{\lambda}_k\frac{\partial F_{1k}}{\partial \sigma_{zz}} \quad \Rightarrow \quad \sum_{i=1}^{3} u_i\xi_i = \sum_{k=1}^{p}\dot{\lambda}_k B_k \tag{7.8b}$$

$$\dot{\gamma}_{xz} = 2\dot{\varepsilon}_{xz} = \frac{\partial v}{\partial x} + \frac{\partial u}{\partial z} = \sum_{i=1}^{3} v_i \frac{\partial N_i}{\partial x} + \sum_{i=1}^{3} u_i \frac{\partial N_i}{\partial z} = \sum_{k=1}^{p} \dot{\lambda}_k \frac{\partial F_{1k}}{\partial \tau_{xz}}$$

$$\Rightarrow \sum_{i=1}^{3} v_i \eta_i + \sum_{i=1}^{3} u_i \xi_i = \sum_{k=1}^{p} \dot{\lambda}_k C_k \tag{7.8c}$$

In matrix form, the following sets of linear equations are generated for any arbitrary element, *e*:

$$\left[a_{11}^e\right]\left\{\boldsymbol{u}^e\right\} + \left[a_{12}^e\right]\left\{\dot{\boldsymbol{\lambda}}^e\right\} = 0 \tag{7.9}$$

where,

$$\left[a_{11}^e\right] = \begin{bmatrix} \eta_1 & 0 & \eta_2 & 0 & \eta_3 & 0 \\ 0 & \xi_1 & 0 & \xi_2 & 0 & \xi_3 \\ \xi_1 & \eta_1 & \xi_2 & \eta_2 & \xi_3 & \eta_3 \end{bmatrix}; \left[a_{12}^e\right] = \begin{bmatrix} -A_1 & -A_2 & ..... & -A_P \\ -B_1 & -B_2 & ..... & -B_P \\ -C_1 & -C_2 & ..... & -C_P \end{bmatrix}$$

$$\left\{\boldsymbol{u}^e\right\}^T = \left\{u_1^e \quad v_1^e \quad u_2^e \quad v_2^e \quad u_3^e \quad v_3^e\right\}; \left\{\dot{\boldsymbol{\lambda}}^e\right\} = \left\{\dot{\lambda}_1^e \quad \dot{\lambda}_2^e \quad ..... \quad \dot{\lambda}_p^e\right\};$$

$$\eta_i = \frac{1}{2A^e}(z_j - z_k); \xi_i = \frac{1}{2A^e}(x_j - x_k); \ \dot{\lambda}_k \geq 0; \ k = 1, 2, \ldots\ldots, p.$$

Thus, pertaining to each element, the velocity compatibility and the normality flow rule results in three equality constraints consisting of six nodal variables (u_i^e, v_i^e) and p numbers of elemental variables ($\dot{\lambda}_i^e$):

7.4.2 Constraints arising from plastic flow along velocity discontinuities

Similar to the plastic straining within the elements, the plastic flow along the velocity discontinuity lines (VDL) is estimated by using MC yield criterion and the AFR. The VDL is the interface between two neighboring elements where a sudden change in velocity (i.e. velocity jump) is permitted. Figure 7.6a describes a typical VDL which is constituted by the nodal pairs (1,2) and (3,4) and makes an angle of ω (anti-clockwise) with horizontal axis. The normal (Δv) and tangential (Δu) velocity jump across the line of discontinuity is obtained as follows:

(a) MC yield envelope (in τ–σ_n space):

$$F_2(\tau,\sigma_n) = |\tau| + \sigma_n \tan\phi - c - \sigma^s \tan\phi = 0 \qquad (7.10)$$

(b) AFR: $|\Delta u| = \dot{\lambda}\left|\frac{\partial F_2}{\partial \tau}\right| = \dot{\lambda}$ and $\Delta v = \dot{\lambda}\frac{\partial F_2}{\partial \tau} = \dot{\lambda}\tan\phi$ (7.11)

(c) Equation (7.11) leads to: $\Delta v = |\Delta u| \tan\phi$ (7.12)

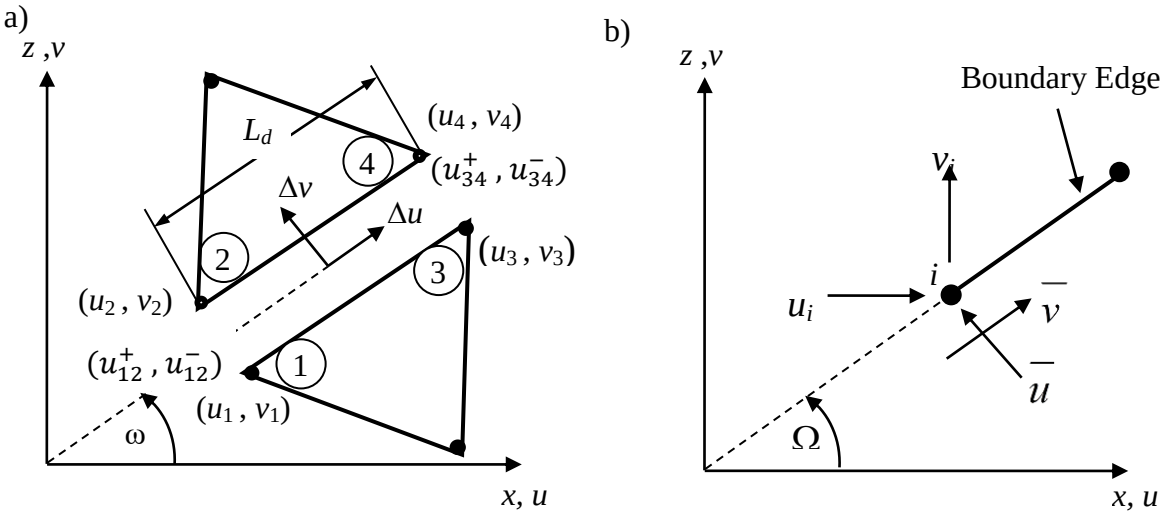

Figure 7.6 a) Nodal velocity variables along the velocity discontinuity; and b) nodal velocities and prescribed velocities on a boundary node, *i*.

In terms of indicial notation Equation (7.12) for any nodal pair (*i*,*j*) is written as:

$$\Delta v_{ij} = |\Delta u_{ij}| \tan\phi \qquad (7.13)$$

Here, $\Delta u_{ij} = (u_j - u_i)\cos\omega + (v_j - v_i)\sin\omega$ and (7.14a)

$$\Delta v_{ij} = (u_i - u_j)\sin\omega + (v_j - v_i)\cos\omega \qquad (7.14b)$$

u_i, u_j, v_i and v_j are the respective nodal velocities.

Since Δu_{ij} is unrestricted in sign and the absolute term in Equation (7.13) prevents the formation of linear programming problem, the following two equations are adopted:

$\Delta u_{ij} = u_{ij}^+ - u_{ij}^-$; where, u_{ij}^+ and u_{ij}^- are two nonnegative variables; (7.15a)

$$\left|\Delta u_{ij}\right| = u_{ij}^{+} + u_{ij}^{-} \quad \Rightarrow \quad \Delta v_{ij} = \left(u_{ij}^{+} + u_{ij}^{-}\right)\tan\phi \tag{7.15b}$$

It is noteworthy that to satisfy Equations (7.15a) and (7.15b) either u_{ij}^{+} or u_{ij}^{-} must be zero.

Combining Equations (7.14a) and (7.15a) and Equations (7.14b) and (7.15b), the following two sets of expressions are obtained for each nodal pair.

For nodal pairs (1, 2): $(u_2 - u_1)\cos\omega + (v_2 - v_1)\sin\omega = u_{12}^{+} - u_{12}^{-}$ (7.16a)

$$(u_1 - u_2)\sin\omega + (v_2 - v_1)\cos\omega = (u_{12}^{+} + u_{12}^{-})\tan\phi \tag{7.16c}$$

For nodal pairs (3, 4): $(u_4 - u_3)\cos\omega + (v_4 - v_3)\sin\omega = u_{34}^{+} - u_{34}^{-}$ (7.16b)

$$(u_3 - u_4)\sin\omega + (v_4 - v_3)\cos\omega = (u_{34}^{+} - u_{34}^{-})\tan\phi \tag{7.16d}$$

In compact form, these constraints can be expressed as: $a_{21}\boldsymbol{x}_1 - a_{23}\boldsymbol{x}_3 = 0$ (7.17)

where, $a_{21} = \begin{bmatrix} T & -T & 0 & 0 \\ 0 & 0 & T & -T \end{bmatrix}_{(4x8)}$; $T = \begin{bmatrix} -\cos\omega & -\sin\omega \\ \sin\omega & -\cos\omega \end{bmatrix}_{(2x2)}$ and

$$a_{23} = \begin{bmatrix} P & 0 \\ 0 & P \end{bmatrix}_{(4x4)}; P = \begin{bmatrix} 1 & -1 \\ \tan\phi & \tan\phi \end{bmatrix}$$

$$\boldsymbol{x}_3 = \left\{u_{12}^{+} \quad u_{12}^{-} \quad u_{34}^{+} \quad u_{34}^{-}\right\}_{(4x1)}^{T}; \boldsymbol{x}_3 \geq 0$$

At the soil footing interface, the value of angle ϕ in a_{23} matrix is being replaced by the interface friction angle, δ.

7.4.3 Constraints arising due to velocity boundary conditions

While constructing KA velocity field, the prescribed velocity boundary conditions are strictly to be satisfied. Figure 7.6b depicts the nodal velocity components at a node *i* on a boundary edge with prescribed tangential and normal velocities, $\bar{u}$ and $\bar{v}$. Resolving the horizontal and vertical velocities along and normal to the boundary edge, the following two equality constraints gets evolved:

$$u_i \cos\Omega + v_i \sin\Omega = \bar{u} \text{ and } -u_i \sin\Omega + v_i \cos\Omega = \bar{v} \tag{7.18}$$

here Ω indicates the inclination angle of the boundary edge. The above constraints can be expressed in the matrix form as:

$$a_{31}\boldsymbol{x}_1 = \boldsymbol{b}_3 \tag{7.19}$$

where, $a_{31} = \begin{bmatrix} \cos\Omega & \sin\Omega \\ -\sin\Omega & \sin\Omega \end{bmatrix}_{(2x2)}$; $\boldsymbol{x}_1 = \{u_i \quad v_i\}^T_{(2x1)}$; $\boldsymbol{b}_3 = \{\bar{u} \quad \bar{v}\}^T_{(2x1)}$

7.4.4 Objective function

The objective function is obtained by equating the rate of the external work done (P_{ext}) with the total internal power dissipation (P_{int}). Two types of external loads are being applied: the traction force and the body force. Hence, the rate of the total work done by the external loads can be expressed as,

$$P_{ext} = \int_A \sigma_n v_n dA + \sum_{e=1}^{E} P_{1e} \tag{7.20}$$

where, (i) σ_n is the traction and v_n is the normal velocity in the direction of σ_n, over the surface area, dA, (ii) P_{1e} provides the rate of work done by the body force within an element, e, and (iii) E is the total number of elements.

The plastic straining induced total internal power dissipation is computed by summing up the power dissipations within the elements as well as along the velocity discontinuities.

$$P_{int} = \sum_{e=1}^{E} P_{2e} + \sum_{d=1}^{D_c} P_{3d} \tag{7.21}$$

where, (i) P_{2e} imparts the power dissipation within an element, e, and (ii) P_{3d} brings forth the power dissipation along VDL, d , and (iii) D_c refers to the total number of VDL.

Equating the expressions of P_{ext} and P_{int} the following resultant equation is obtained:

$$P_{ext} = \int_L \sigma_n v_n dL + \sum_{e=1}^{E} P_{1e} = P_{int} = \sum_{e=1}^{E} P_{2e} + \sum_{d=1}^{D_c} P_{3d} \tag{7.22}$$

For rigid footing, v_n can be moved out from the integration because the normal velocity becomes constant over the loaded boundary. Therefore, the applied total normal force (Q_u) can be computed by using the following equation.

$$Q_u = \int_L \sigma_n dL = \left(\sum_{e=1}^{E} P_{2e} + \sum_{d=1}^{D_c} P_{3d} - \sum_{e=1}^{E} P_{1e} \right) / v_n \tag{7.23}$$

The chosen value of v_n has no influence on Q_u.

In the following sections, the expressions of P_{1e}, P_{2e} and P_{3d} are discussed elaborately.

7.4.4.1 The rate of work done by the body forces

For a given triangular element, *e*, the expression of P_{1e} is obtained by multiplying the magnitude of body force with the average of the vertical velocities. This is expressed as:

$$P_{1e} = -\frac{\gamma A^e}{3}(v_1 + v_2 + v_3) \tag{7.24}$$

where v_i's are the vertical velocities at node *i*. The negative sign is ascribed to the equation owing to the fact that the soil's unit weight, γ, acts in the downward direction and v_i is positive upward.

In the matrix form, this equation can be represented as: $P_{1e} = \boldsymbol{c}_1^T \boldsymbol{x}_1$ (7.25)

where, $\boldsymbol{c}_1^T = \left(\frac{\gamma A^e}{3} \right) \begin{bmatrix} 0 & 1 & 0 & 1 & 0 & 1 \end{bmatrix}$ and $\boldsymbol{x}_1 = \{ u_1 \quad v_1 \quad u_2 \quad v_2 \quad u_3 \quad v_3 \}^T_{(6x1)}$

7.4.4.2 Power dissipation in continuum due to plastic deformation

Due to plastic flow, the power dissipation throughout an arbitrary element, *e*, can be computed as follows:

$$P_{2e} = \int_{A^e} (\sigma_{xx}\dot{\varepsilon}_{xx} + \sigma_{zz}\dot{\varepsilon}_{zz} + \tau_{xz}\dot{\gamma}_{xz})dA \tag{7.26}$$

Plugging the expressions of the plastic strain rates into the above equation, the power dissipation throughout a triangular element can be expressed in the following form:

$$P_{2e} = \int_{A^e} \left\{ \sum_{k=1}^{p} \dot{\lambda}_k (A_k \sigma_{xx} + B_k \sigma_{zz} + C_k \tau_{xz}) \right\} dA = 2(c\cos\phi - \sigma^s \sin\phi) A^e \sum_{k=1}^{p} \dot{\lambda}_k \tag{7.27}$$

It can be well noted that the variation of the yield surface size and the plastic multiplier associated with the assumed linearized polygon combinedly contribute to the rate of plastic power dissipation of an element.

In matrix form, the power dissipation within an element can be written as:

$$P_{2e} = \boldsymbol{c}_2^T \boldsymbol{x}_2 \tag{7.28}$$

where, $\boldsymbol{c}_2^T = 2(c\cos\phi - \sigma^s \sin\phi) A^e \begin{bmatrix} 1 & \dots & 1 & \dots & 1 & \dots & 1 & \dots & 1 \end{bmatrix}_{(1\times p)}$

$\boldsymbol{x}_2 = \left\{ \dot{\lambda}_1 \quad \dots\dots\dots \quad \dot{\lambda}_k \quad \dots\dots\dots \quad \dot{\lambda}_p \right\}^T$; $\boldsymbol{x}_2 \geq 0$

Considering the complementarity condition (i.e., $\dot{\lambda}_k F_{1k} = 0$) and the non-negativity of the plastic multiplier, it can be inferred that all the $\dot{\lambda}_k$ are zero for the elements which are not yielded. This eventually implies that the value of P_{2e} will be non-zero corresponding to those triangular elements that lie within the inelastic zone.

7.4.4.3 Power dissipation along the velocity discontinuities

Obeying the associative flow rule, the power dissipation along the velocity discontinuity line, of length L_d, can be expressed as follows:

$$P_{3d} = \int_{L_d} (|\tau \Delta u| + \sigma_n \Delta v) dl \tag{7.29}$$

By using Equation (7.20), Equation (7.37) can be expressed as:

$$P_{3d} = \int_{L_d} \{ |\Delta u| (|\tau| + \sigma_n \tan\phi) \} dl \tag{7.30}$$

For unsaturated soil, considering the tensile stress to be positive the extended form of the MC yield envelope in $\tau - \sigma_n$ stress space can be rewritten as:

$$P_{3d} = \int_{L_d} \left\{ |\Delta u| (c - \sigma^s \tan\phi) \right\} dl \tag{7.31}$$

In terms of matrix form, this can be expressed as: $P_{3d} = \boldsymbol{c}_3^T \boldsymbol{x}_3$ (7.32)

where, $\boldsymbol{c}_3^T = \dfrac{L_d (c - \sigma^s \tan\phi)}{2} \begin{bmatrix} 1 & 1 & 1 & 1 \end{bmatrix}$

$$\boldsymbol{x}_3 = \begin{Bmatrix} u_{12}^+ & u_{12}^- & u_{34}^+ & u_{34}^- \end{Bmatrix} \; ; \; \boldsymbol{x}_3 \geq 0$$

One can clearly observe, as demonstrated in Figure 7.6b, that how the intercept of the yield envelope in the τ axis grows/shrinks in size with the variations in suction stress and eventually makes an impact in evaluating the power dissipation along the velocity discontinuity.

7.4.4.4 Assembling the constraint equations and objective function

After constructing the kinematically admissible velocity field, the objective function is obtained by equating the rate of the total work done by the external loads to the total internal power dissipation. The equality and nonequality constraints are further assembled, and the canonical form of the linear optimization problem can be stated as follows:

Minimize objective function: $\boldsymbol{C}_2^T \boldsymbol{X}_2 + \boldsymbol{C}_3^T \boldsymbol{X}_3 - \boldsymbol{C}_1^T \boldsymbol{X}_1$ (7.33)

$$\text{Subjected to:} \quad \begin{matrix} 3E \text{ rows} \rightarrow \\ 4D_c \text{ rows} \rightarrow \\ 2N_b \text{ rows} \rightarrow \end{matrix} \begin{bmatrix} \boldsymbol{A}_{11} & -\boldsymbol{A}_{12} & \boldsymbol{0} \\ \boldsymbol{A}_{21} & \boldsymbol{0} & -\boldsymbol{A}_{23} \\ \boldsymbol{A}_{31} & \boldsymbol{0} & \boldsymbol{0} \end{bmatrix} \begin{Bmatrix} \boldsymbol{X}_1 \\ \boldsymbol{X}_2 \\ \boldsymbol{X}_3 \end{Bmatrix} = \begin{Bmatrix} \boldsymbol{B}_1 \\ \boldsymbol{B}_2 \\ \boldsymbol{B}_3 \end{Bmatrix} ; \; \boldsymbol{X}_2 \geq 0 \; ; \; \boldsymbol{X}_3 \geq 0 \tag{7.34}$$

$$\begin{matrix} 2N \uparrow & pE \uparrow & 4D_c \uparrow \\ \text{columns} & \text{columns} & \text{columns} \end{matrix}$$

where,

$$\boldsymbol{C_1} = \left\{ \sum_{e=1}^{E} \boldsymbol{c}_1^e \right\}_{(2N\times 1)} \quad ; \qquad \boldsymbol{C_2} = \left\{ \sum_{e=1}^{E} \boldsymbol{c}_2^e \right\}_{(pE\times 1)} \quad ; \qquad \boldsymbol{C_3} = \left\{ \sum_{dc=1}^{D_c} \boldsymbol{c}_3^{dc} \right\}_{(4D_c\times 1)} \tag{7.35a}$$

$$\boldsymbol{A_{11}} = \left[\sum_{e=1}^{E} a_{11}^e \right]_{(3E\times 2N)} \quad ; \qquad \boldsymbol{A_{12}} = \left[\sum_{e=1}^{E} a_{12}^e \right]_{(3E\times pE)} \quad ; \qquad \boldsymbol{A_{21}} = \left[\sum_{dc=1}^{D_c} a_{21}^{dc} \right]_{(4D_c\times 2N)}$$

(7.35b)

$$\boldsymbol{A_{23}} = \left[\sum_{dc=1}^{D_c} a_{23}^{dc} \right]_{(4D_c\times 4D_c)} \quad ; \qquad \boldsymbol{A_{31}} = \left[\sum_{bd=1}^{N_b} a_{31}^{bd} \right]_{(2N_b\times 2N)} \quad ; \qquad \boldsymbol{B_3} = \left\{ \sum_{bd=1}^{N_b} \boldsymbol{b}_3^{bd} \right\}_{(2N_b\times 1)} \tag{7.35c}$$

Here, i) $\boldsymbol{X_1}$ = global vector of the nodal velocities (unbounded)

$\boldsymbol{X_2}$ = global vector of the element plastic multiplier rates (positive)

$\boldsymbol{X_3}$ = global vector of the velocity discontinuity parameters (positive)

ii) $\boldsymbol{A_{ij}}$ and $\boldsymbol{B_i}$'s are the component of the global coefficient matrix and the right-hand side vector that are evolved from the equality constraints; (a) $\boldsymbol{A_{11}}$, $\boldsymbol{A_{12}}$, and $\boldsymbol{B_1}$ are generated from the constraints associated with the plastic flow in the continuum, (b) $\boldsymbol{A_{21}}$, $\boldsymbol{A_{23}}$, and $\boldsymbol{B_2}$ are generated from the velocity discontinuity constraint following the associated flow rule and (c) $\boldsymbol{A_{31}}$, and $\boldsymbol{B_3}$ are generated by satisfying the velocity boundary conditions.

iii) $\boldsymbol{C_2}$ and $\boldsymbol{C_3}$ are the global vector of the coefficients arising from the power dissipation within the continuum element and along the velocity discontinuity, respectively and $\boldsymbol{C_1}$ are the global vector of the coefficients arising due to the consideration of the work done by the body forces.

7.4.5 Solution procedure for linear optimization

The upper bound formulations are sufficiently modified to accommodate the spatial variation of the 3-D yield surface. The consideration of suction stress on (a) yield circle's size, (b) yield envelope's position, and (c) power dissipation terms are first of its kind. For performing the numerical simulations, the computer programs are written

in MATLAB (R2019a) and large-scale interior point solver (LIPSOL) algorithm, namely, '*LINPROG*' available in MATLAB's library is utilized for performing the required linear optimization. The detailed computational procedure is described in Sloan and Kleeman (1995) and Kumar and Kouzer (2007). To run '*LINPROG*', the following command can be used:

$$\boldsymbol{X} = \textbf{linprog}\ (\boldsymbol{C, A_{ineq}, B_{ineq}, A_{eq}, B_{eq}, LB, UB}) \tag{7.36}$$

The coefficients of linear inequality constraints are represented by the matrix $\boldsymbol{A_{ineq}}$ and vector $\boldsymbol{B_{ineq}}$, i.e., $\boldsymbol{A_{ineq}X \leq B_{ineq}}$. Since no inequality constraints are present in the current study, A_{ineq} and B_{ineq} were set to empty matrices, while $\boldsymbol{A_{eq} = A}$ and $\boldsymbol{B_{eq} = B}$. The parameters *LB* and *UB* define the lower and upper bounds on the variable *X* so that the solution always falls within the range of $\boldsymbol{LB \leq X \leq UB}$. As the unknown matrix X_1 is unbounded and X_2, $X_3 > 0$, the solution falls within those parameters, therefore,

$$LB = \begin{Bmatrix} -\infty & 0 & 0 \end{Bmatrix}^T \text{ and } LB = \begin{Bmatrix} +\infty & +\infty & +\infty \end{Bmatrix}^T \tag{7.37}$$

The limit analysis technique provides rigorous solutions without any prior assumption of the failure surface. Furthermore, unlike the displacement based finite element technique, UB-FELA do not require any step-by-step elasto-plastic analysis and a complete constitutive model; therefore, this technique is time saving and cost effective process.

7.5 NUMERICAL EXAMPLE:- BEARING CAPACITY OF STRIP FOOTING ON UNSATURATED SANDY SOIL

7.5.1 Problem statement and Domain

A rigid strip footing of width, *B*, is placed over homogenous frictional soil, as shown in Figure 7.7a. The load over the strip footing is considered to be vertical and concentric. The water table is at a depth of h_w below the ground surface. The soil below and above the water table is considered to be completely saturated and variably

saturated, respectively. The variations of matric suction with respect to *y* are shown in Figure 7.7a for three flow conditions. The suction stress based effective stress is used in formulating the problem. It is intended to evaluate the bearing capacity of the strip footing by varying the position of the water table in presence as well as in absence of vertical surcharge pressure with the aid of upper bound limit analysis in association with finite elements and linear optimization.

Owing to the symmetricity of the footing, only one-half of the concerned region about the central axis of the footing is considered in present analysis. The boundary of the chosen region is marked as ABCD in Figure 7.7a. The size of the domain is chosen to be large enough such that the following two conditions are met: (a) solution does not get affected by any further extension of size of domain and (b) the nodal pattern remains completely within the domain. Considering these two criteria, the vertical and the horizontal extent of the domain are chosen as 4–16*B* and 5–20*B* respectively. The considered domain and the associated boundary conditions are depicted in Figure 7.7b. The imposed boundary conditions are as follows: (1) along the central axis (AB), horizontal velocity is made to be zero due to the symmetricity, (2) along the bottom (BC) and the right side (CD) boundaries, displacements are restricted in both directions, and (3) along the base of the footing (AN) vertical velocity is specified with a specific value and proper direction and horizontal velocity is controlled by the soil–footing roughness angle (δ), which was either considered to be zero (perfectly smooth) or perfectly rough (ϕ).

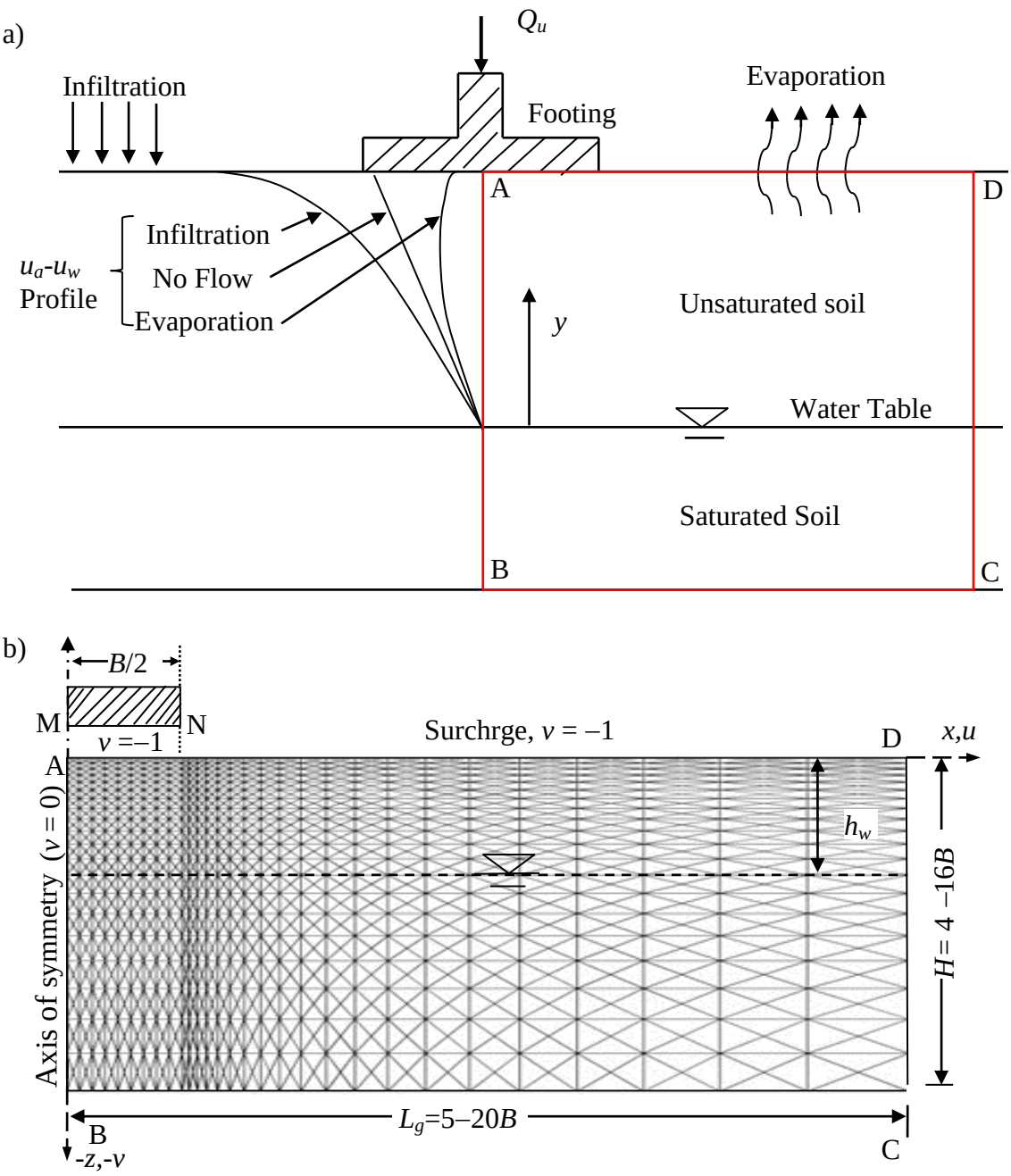

Figure 7.7 a) Strip footing rested over unsaturated sandy layer; b) Choosen domain with mesh.

7.5.2 Results and Discussion

The computations were performed for various combinations of mechanical strength (ϕ), vG SWRC model parameters (α, n, and m), flow conditions (no-flow, evaporation, and precipitation), flow rate (q), water table depth (h_w) measured from the ground surface, and surcharge pressure (q_s). Four different ϕ values, namely, 30°, 35°,

40°, and 45° are chosen corresponding to different α (0.1, 0.3, 0.5, 0.7, and 0.9 kPa^{-1}), n (2, 4, 6, and 8) parameters, n and m relationships (K_M = 0, 2, and 4). The hydromechanical parameters that are selected in view of the fact that sands are placed beneath the footing. The collapse loads are computed by varying the water table depth with and without the presence of surcharge pressure. Following Terzaghi's (1943) classical formulation, the bearing capacity expression of the strip foundation can be written as:

$$p_u = q_s N_{qs} + 0.5\gamma B N_{\gamma s} \tag{7.38}$$

where, N_{qs} and $N_{\gamma s}$ are the bearing capacity factor (BCF) with respect to the surcharge pressure and unit weight; the subscript s indicates that the effect of suction stress is duly considered. The BCF are obtained by assuming the validity of the superposition principle; for determining N_{qs} and $N_{\gamma s}$ the soil is considered to be (a) weightless with surcharge pressure (q_s) and (b) ponderable without surcharge pressure, respectively.

Figure 7.8 shows the variation of BCF with respect to the water table fluctuation for ϕ =30° soil. The curves are drawn for various values of α corresponding to K_M =0 and for four n, namely, n =2, n =4, n =5, and n =8. It can be well observed that with the lowering of the water table, both the $N_{\gamma s}$ and N_{qs} parameters initially increases upto a certain h_w and attains a pronounced peak point, thereafter the BCF value falls at a significant rate. After the attainment of the peak point, the rate of decrement of the $N_{\gamma s}$ curve becomes sharper with the increase in n. The depth of water table at which the BCF attains maximum value is referred

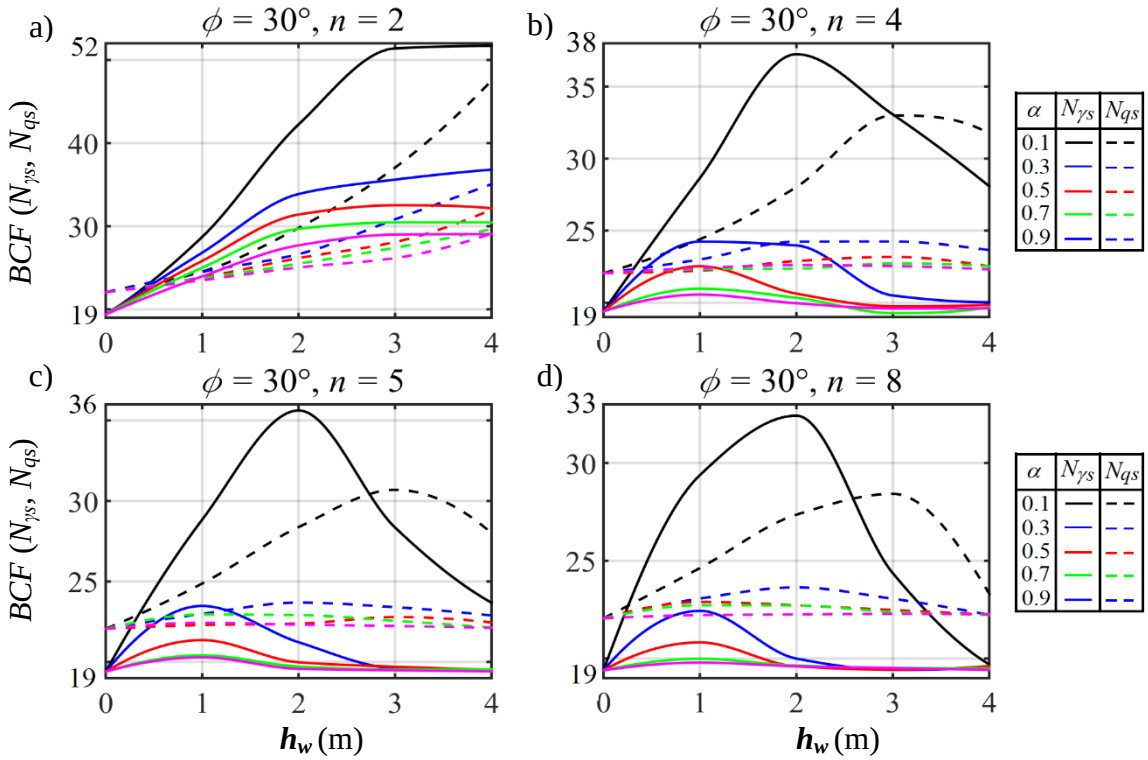

Figure 7.8 The variation in $N_{\gamma s}$ and N_{qs} for sandy soil with ϕ=30° and K_M=0 and that correspond to five α's and four different values of: a) n=2; b) n=4; c) n=5; and d) n=8.

here as critical position of water table (h_{wcr}). The h_{wcr} appears earlier for $N_{\gamma s}$ in comparison to its N_{qs} counterpart. When the water table reaches below the ground surface, the BCF becomes almost same as the saturated soil. The presence of h_{wcr} is more prominent for higher n (=4, 5, and 8) and the lowest chosen α (i.e. α =0.1). However, when n is equal to 2, the presence of peak point in the BCF curves within the selected range of h_w is not observable. Instead N_{qs} increases continuously with the increase in h_w and the $N_{\gamma s}$ parameter reaches to a horizontal plateau after a certain h_w. For ϕ =30° soil, when the water table rises upto the ground surface (i.e. the soil is completely saturated), the magnitude of N_{qs} is greater than $N_{\gamma s}$, nonetheless, as water table goes down either the N_{qs} curve is positioned below the $N_{\gamma s}$ (for α=0.1 and/or lower n) or N_{qs} curve lie above the $N_{\gamma s}$ (for α >0.5 and poorly graded soil). The friction angle

also plays a certain role in determining the h_{wcr}, especially for high α. For instance, corresponding to α=0.9, (i) when n=4, h_{wcr} equals to 0.8 and 3 for ϕ=30° and ϕ=45°, respectively, and (ii) when n=8, h_{wcr} equals to 1.1 and 2 for ϕ=30° and ϕ=45°, respectively.

Figures 7.9, 7.10, and 7.11 display the variation of BCF with h_w corresponding to K_M =0, K_M =2, and K_M =4, respectively. The figures are drawn for three different frictional strength (ϕ =35°, 40°, and 45°) by varying the SWRC model parameters. Irrespective of ϕ, the BCF remains always higher for lower n and high AEV, nevertheless, the prominence of the presence of h_{wcr} diminishes as the strength of the soil increases. The magnitude of h_{wcr} also seems to be affected by the value of α; as α increases, the maximum bearing capacity is obtained near the ground surface. The $N_{\gamma s}$ curves, generated for various values of α, come closer to each other with the increase in pore spectrum number and mechanical shear strength. It is also noticeable that for stronger soil with uniformly distributed pore space, the deviation of the $N_{\gamma s}$ and N_{qs} curves increases to a significant extent. Furthermore, the BCF curves generated for α >0.5 and n ≥4 do not get influenced much by the fluctuation of water table. With the increase in strength of the soil, the BCF curves become almost indifferent to the rising/lowering of water table. The bearing capacity also remains independent of flow condition as the suction stress does not depend on flow condition. However, the roughness condition of the soil-footing interface (indicated by angle δ) impacts the load-bearing capacity to a great extent. Table 7.1 presents the $N_{\gamma s}$ factor for various combinations of α, n, ϕ, and h_w corresponding to three different δ/ϕ, namely,

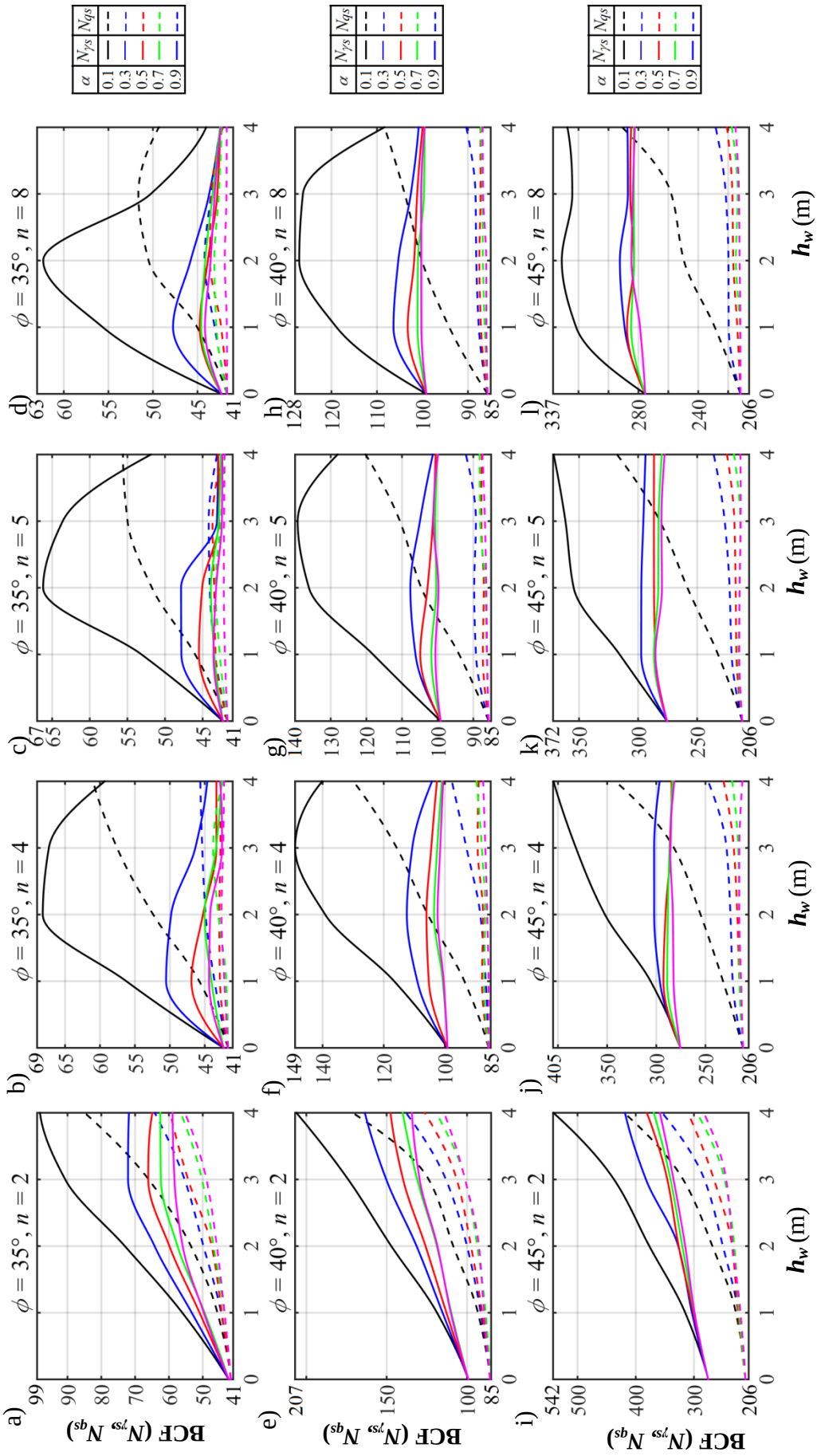

Figure 7.9 The variation in $N_{\gamma s}$ and N_{qs} for sandy soil that had different combinations of α and n that correspond to K_M=0 and for four different values of: (a–d) ϕ=35°; (e–h) ϕ=40°; and (i–l) ϕ=45°.

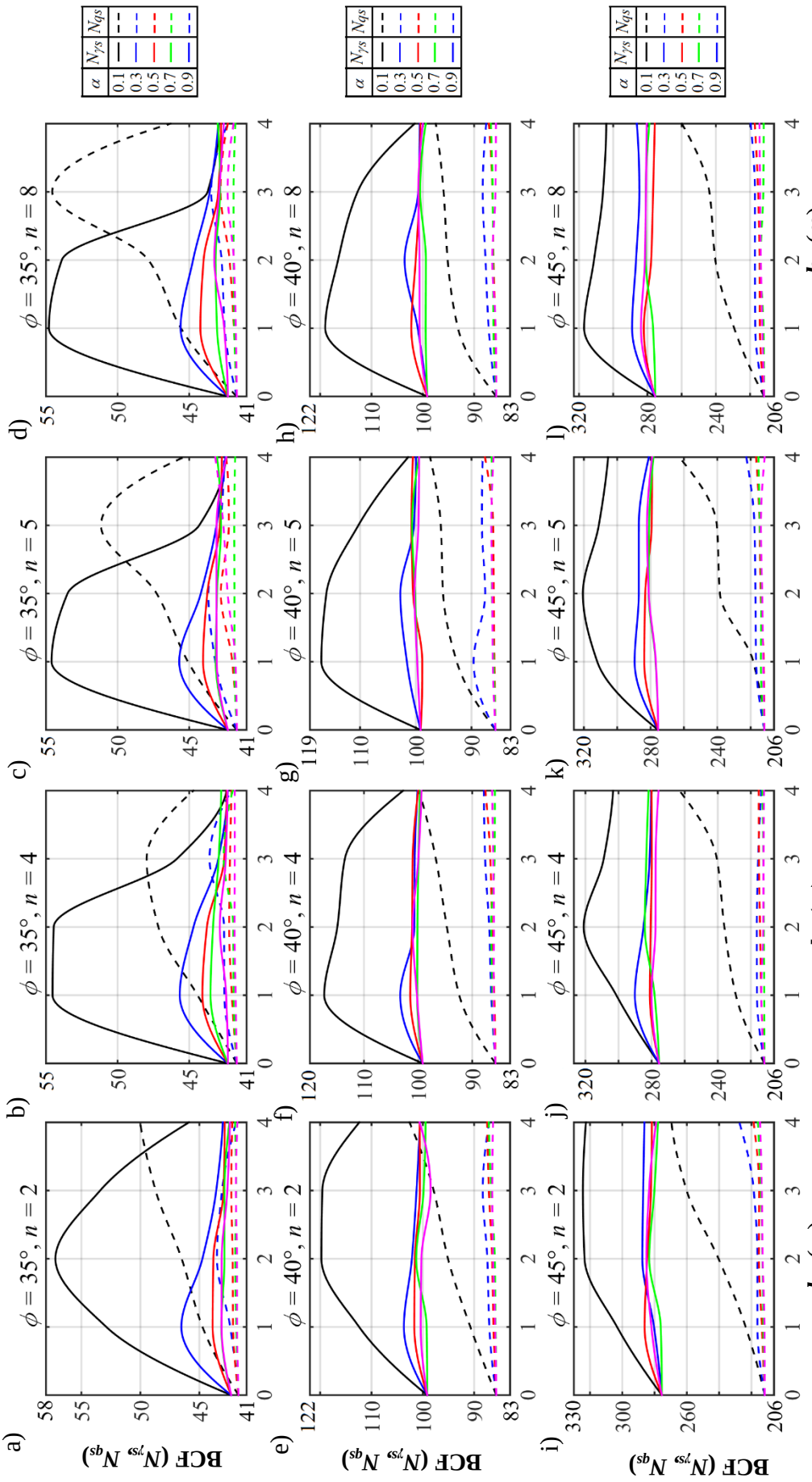

Figure 7.10 The variation in $N_{\gamma s}$ and N_{qs} for sandy soil that had different combinations of α and n that correspond to K_M =2 and for four different values of: (a–d) ϕ=35°; (e–h) ϕ=40°; and (i–l) ϕ=45°.

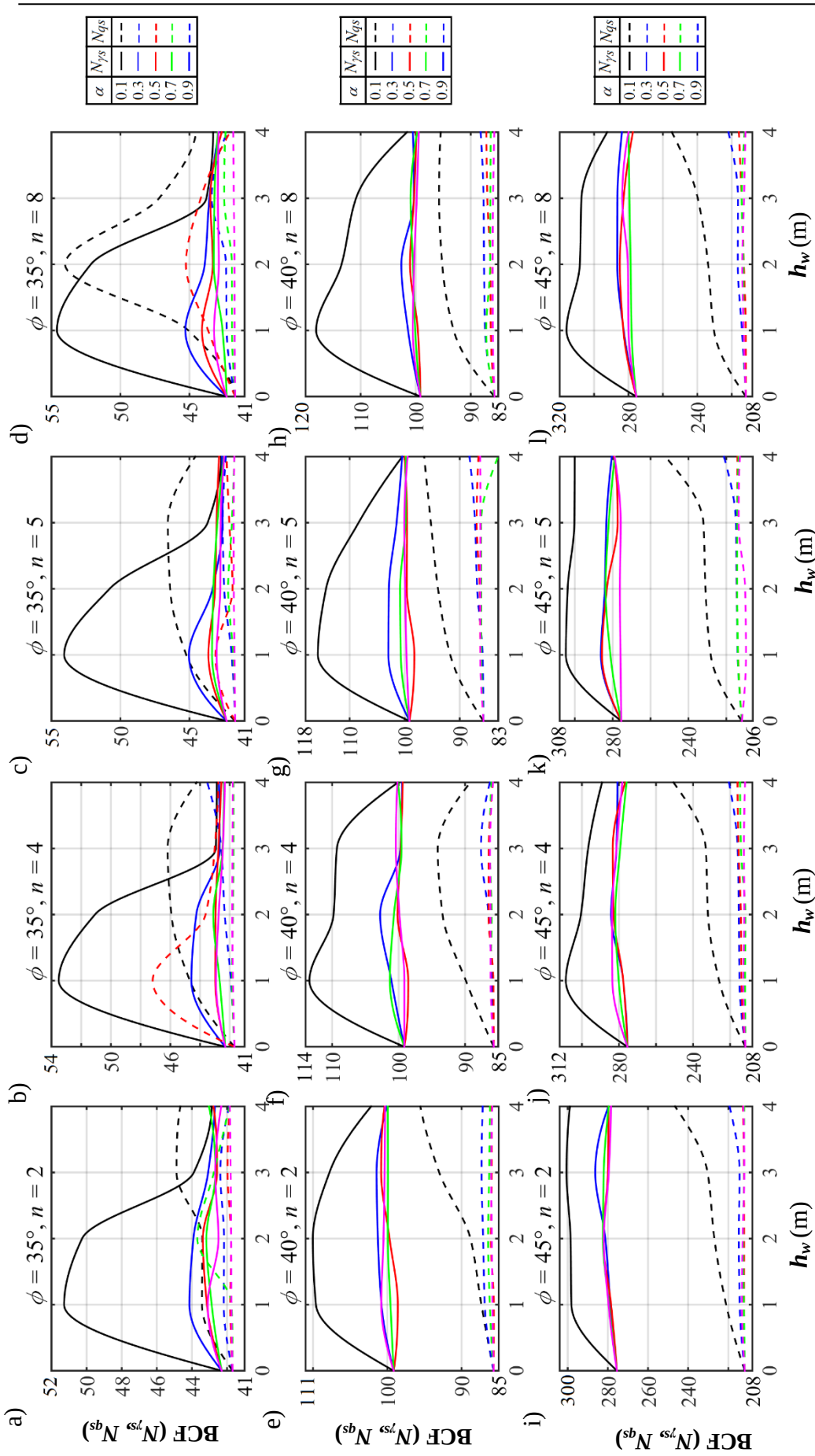

Figure 7.11 The variation in $N_{\gamma s}$ and N_{qs} for sandy soil that had different combinations of α and n that correspond to K_M=4 and for four different values of: (a–d) ϕ=35°; (e–h) ϕ=40°; and (i–l) ϕ=45°.

Table 7.1 The variation of $N_{\gamma s}$ for K_M=0 and different values of n, α, ϕ, and δ/ϕ.

n	α	h_w	ϕ=30°			ϕ=40°		
			δ/ϕ=0	0.5	1	0	0.5	1
4	0.1	0	11.59	20.14	21.98	67.62	138.87	147.49
		1	27.98	33.23	32.48	104.56	175.99	173.43
		2	25.19	40.86	42.21	133.50	206.33	207.01
		3	20.20	33.78	37.47	116.37	217.71	221.64
		4	18.64	28.44	31.82	98.20	197.43	208.40
	0.5	0	11.59	20.14	21.98	67.62	138.87	147.49
		1	14.57	23.80	25.54	78.53	147.68	156.59
		2	12.13	20.94	23.38	72.88	149.39	157.71
		3	11.61	20.56	22.39	69.19	147.75	155.40
		4	14.44	19.70	21.90	68.25	143.65	147.62
8	0.1	0	11.59	20.14	21.98	67.62	138.87	147.49
		1	29.76	33.55	33.30	108.22	175.82	176.87
		2	16.72	31.23	36.74	106.30	191.42	189.07
		3	12.05	21.99	24.74	76.24	177.82	187.85
		4	13.45	20.33	21.60	68.60	152.37	161.21
	0.5	0	11.59	20.14	21.98	67.62	138.87	147.49
		1	12.44	21.56	23.60	72.66	146.97	153.60
		2	12.10	20.17	22.22	68.30	146.15	151.48
		3	11.78	19.61	22.02	66.59	140.98	150.49
		4	11.71	20.14	22.23	67.96	136.89	146.73

δ/ϕ=0, δ/ϕ=0.5, and δ/ϕ=1 and K_M =0. It is quite evident that with the increase in footing roughness BCF increases significantly; nevertheless, this increment is not appreciable when δ/ϕ varies from 0.5 to 1. This indicates that the variation of $N_{\gamma s}$ with respect to the

footing roughness is highly nonlinear. In addition to that, the position of h_{wcr} goes down with the increase in δ/ϕ. Lowering of the critical water table position for the rough footing, in comparison to its smooth counterpart, is far more significant for higher α and poorly graded soil.

The influence of K_M on the estimation of stability can be represented by analyzing Figures 7.9, 7.10, and 7.11. The higher the value of K_M, lower is the BCF. This can be attributed to the fact that as K_M increases, suction stress decreases and so does the BCF. Furthermore, with the increase in K_M, the peak point on the $N_{\gamma s}$ curves losses its prominence and moves closer to the ground surface. However, the magnitude of K_M does not have much influence on the deviations between $N_{\gamma s}$ and N_{qs} curves. The water table depth at which the BCF of the unsaturated soil becomes same as that of saturated soil reduces with the increase in K_M. These observations clearly shows that not only the mechanical strength property of the sands but the water table depth as well as the unsaturated soil properties along with the footing roughness play an important role in governing the bearing capacity of the strip foundation.

Figure 7.12 represents the variation of BCF with α corresponding to K_M =0 and ϕ=35° and 45°. The figures are plotted for four different n values (=2, 4, 5, and 8) and various water table position (h_w= 0, 1, 2, 3 and 4). The pink lines (h_w=0) in the figure are unaffected by α as these lines indicate the saturation state. All other curves corresponding to the unsaturated soils appear to be highly nonlinear. Irrespective of n and ϕ, the BCF curves drop sharply as the value of α increase from 0.1 to 0.3. The rate of the decrement appears to be higher when the water table is positioned at h_{wcr}. Beyond α=0.3, the curves decline at a relatively slower rate. The curves corresponding to the soils with larger n and higher strength become almost flat for α>0.3.

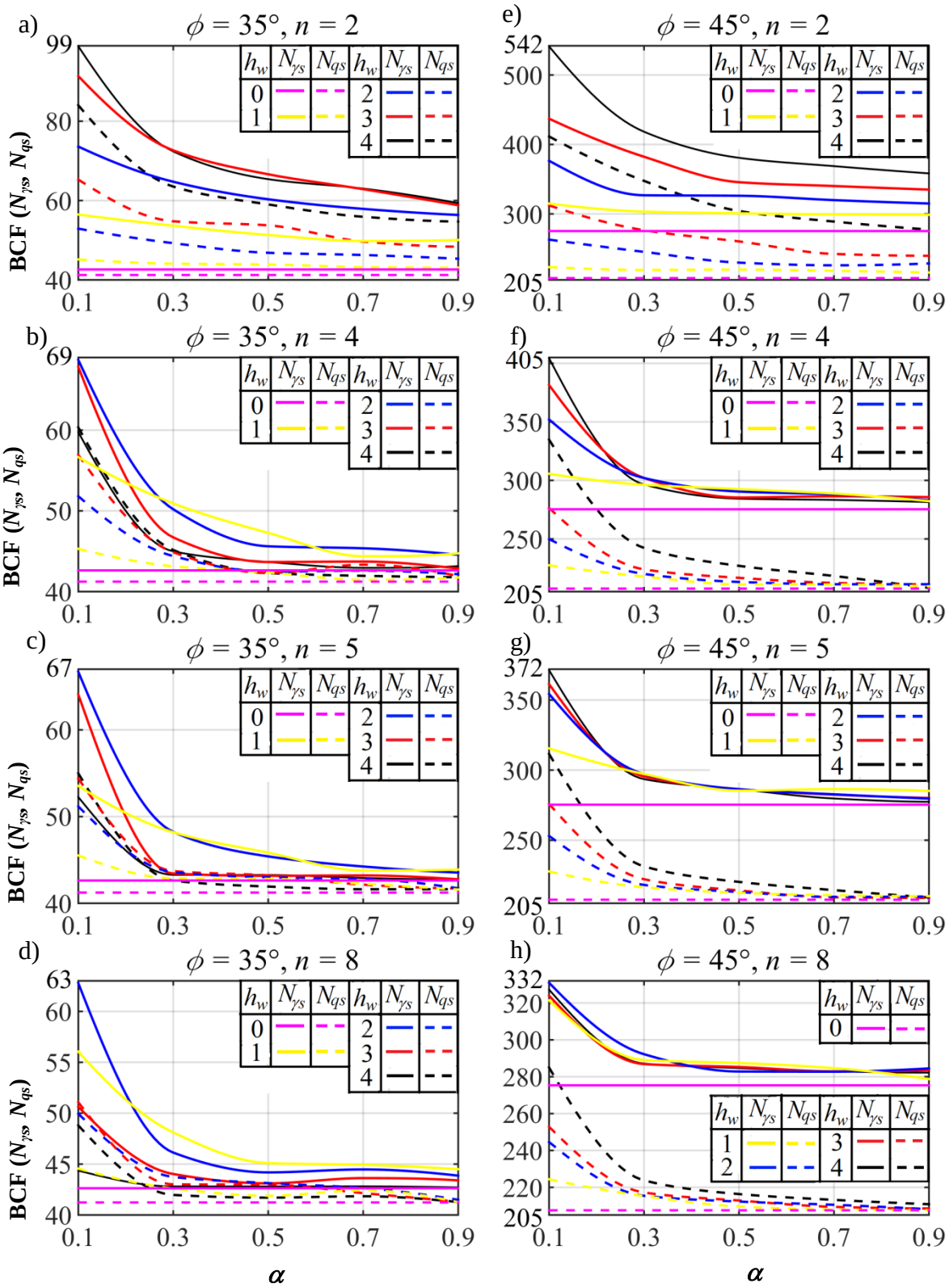

Figure 7.12 The variation in $N_{\gamma s}$ and N_{qs} for sandy soil (ϕ=35°, 45°) with respect to α for different value of h_w that corresponds to K_M=0 and four different values of: a) ϕ=35°, n=2; b) ϕ=35°,n=4; c) ϕ=35°,n=5; d) ϕ=35°,n=8; e) ϕ=45°, n=2; f) ϕ=45°,n=4; g) ϕ=45°,n=5; h) ϕ=45°,n=8.

7.3.2 Nodal velocity patterns

The nodal velocity patterns present the information of the magnitude and direction of soil particle movement at various nodal points within the soil domain. By varying the water table depth, the nodal velocity pattern for strip footing resting on sandy soil having ϕ =35°, α =0.1, and n =4 is drawn and are presented in Figure 7.13; Figures 7.13a–7.13c is associated with $N_{\gamma s}$, whereas, Figure 7.13d–7.13f corresponds to the determination of N_{qs}. The velocities along the ground surface adjacent to the footing edge are found to be significantly higher than the soil mass velocities beneath the footing surface. Moreover, the prominence of the velocity discontinuities is remarkably noticeable around the footing edge and these discontinuities gradually diminish while moving away far from the footing edge. Irrespective of the hydromechanical properties, a curvilinear zone (referred here as influential zone) is developed around the footing edge wherein the nodal velocities are significantly higher than the rest of the soil portion. The horizontal and the vertical extent as well as the magnitudes of the velocity vectors within the influential zone, especially at the ground surface near footing edge, describes the reason of the variation of BCFs.

It is notably visible that as the water table goes down 2 m below the ground surface, the size of the influence zone increases distinctively, whereas, when the water table further lowers down to 4m below the ground surface, the size of the influence zone becomes equal or slightly smaller than that of the saturated counterpart. This explains the formation of "inverted V-shaped" BCF curves and the subsequent existence of the peak point. Apart from the size of the influence zone, the velocity magnitudes on the ground surface adjacent to the footing edge also get altered by the water table fluctuations. Compare to the velocity contour corresponding to the N_{qs}, the nodal velocity pattern pertains to $N_{\gamma s}$ encompasses larger portion of the soil mass; however,

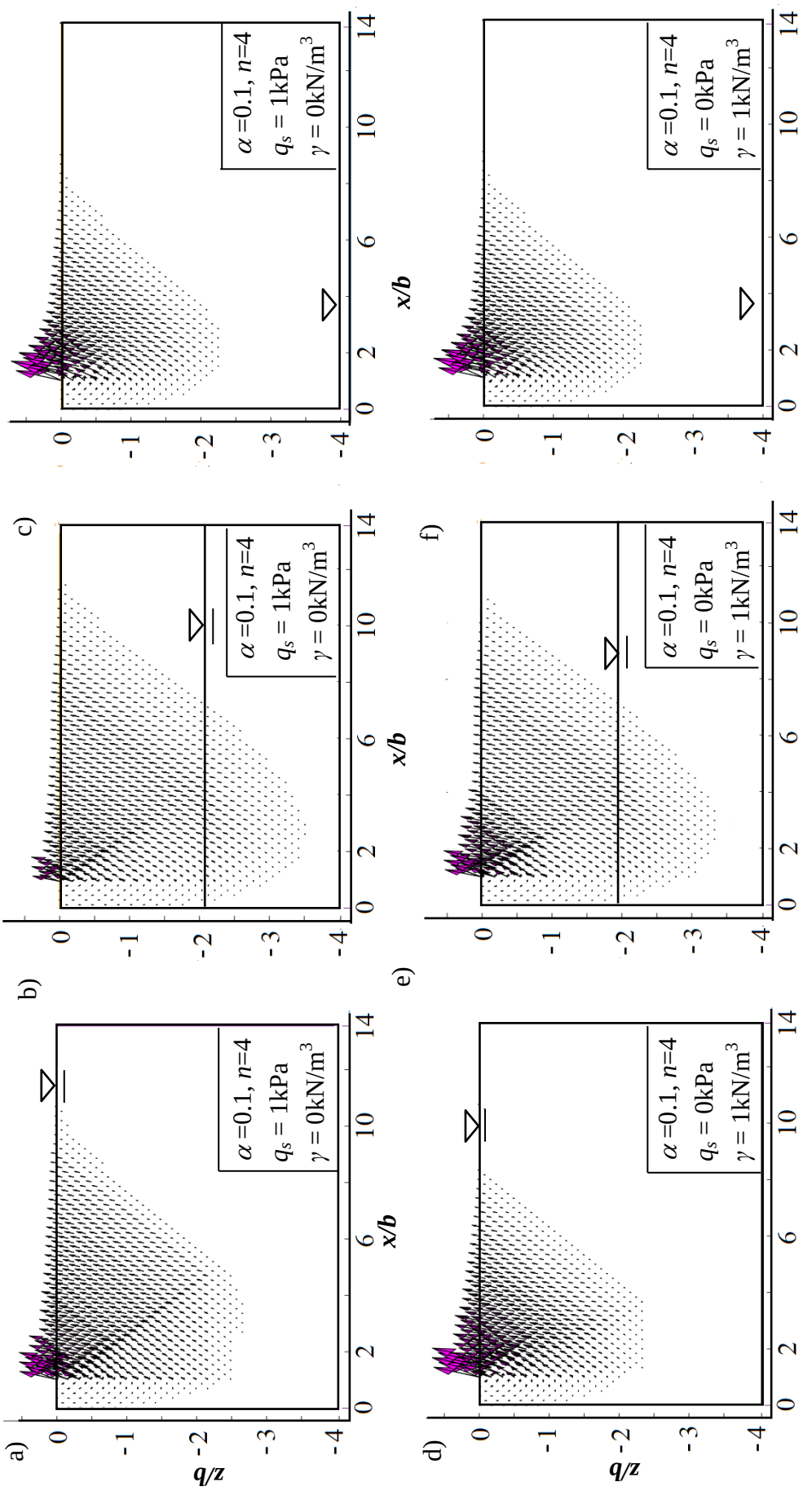

Figure 7.13 Nodal velocity patterns for strip footing that rested on unsaturated sands with ϕ=35° for varying water table positions (h_w/b=0, 2, and 4) that correspond to: (a–c) ponderable surcharge-less soil; and (d–f) weightless soil with surcharge.

the velocity vectors near the footing edge are of higher magnitude during the determination of N_{qs}.

Figure 7.14 presents the change in nodal velocity contour as the pore size distribution of the unsaturated homogenous soil section varies. The chosen soil is of ϕ= 40º, α=0.1, and the water table is 2m below the ground surface. As the soil becomes poorly graded the following three observations are noted: (a) the volume of the influential zone decreases, (b) the nodal velocities near the footing edge increases, and (c) the distinction between the nodal velocity zones become more perceptible.

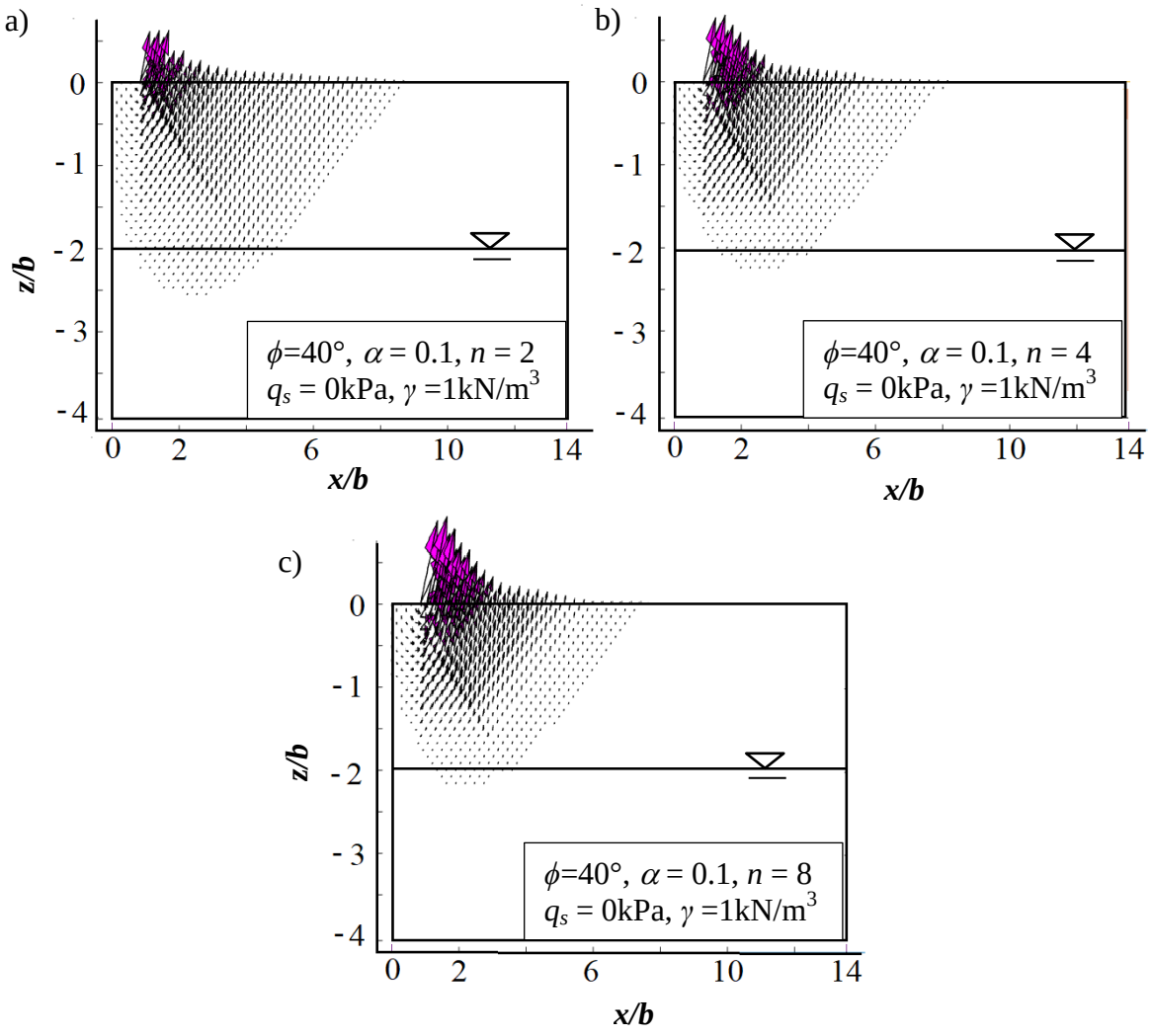

Figure 7.14 Nodal velocity pattern for strip footing on sandy soil (ϕ= 40º) for different n values: a) n= 2; b) n= 4; and c) n=8.

Figure 7.15 depicts the nodal velocity pattern of strip footing resting on ponderable sandy soil (ϕ =40º) for three different α values, namely, α =0.1, α =0.5, and α =0.9 kPa^{-1}. These contours are plotted corresponding to n =4 and h_w/b =2m. With the increase in α parameter, the volume of the influential zone shrinks and the velocity vectors concentration near the footing edge enhances notably. Contrast to Figure 7.13, the diminishing of the velocity concentration is not gradual; rather, three specific zones seem to be identifiable where the velocity vectors have almost the same values. The distinction of these zones becomes more discernible as the saturation regime in the SWRC curve decreases.

Figure 7.16 provides the diagrammatic representation of how the nodal velocity contour reorients as the K_M value is chosen differently, namely, 0, 2, and 4. The variation in the nodal contour is pronounced when K_M changes from 0 to 2 but not appreciable when K_M changes from 2 to 4. This observation justifies the reason of the sustained BCF if K_M is considered greater than 2.

7.3.3 Comparisons of results

Figures 7.9–7.11 clearly reveal that the BCF corresponding to unsaturated soil is quite higher in comparison to the fully saturated soils; for n =2, BCF is found to be 2.5-4 times higher, whereas, for n =8 the rise in BCF is about 2 times. Steensen-Bech et al. (1987), Nabil (1985) and Fathi and Vanapalli (2006) also observed similar trend in the partially saturated zone. Nabil (1985) reported 3 to 5 times increase in bearing capacity, while Fathi and Vanapalli (2006) showed in their study a 5 to 7 times increase in bearing capacity. Table 7.2 presents the solutions reported by (i) Du et al. (2021) on the basis of upper bound limit analysis with discretization techniques and ii) Vahedifard and Robinson (2016) by using unified method by combining Terzaghi's effective stress with suction matric. Following these literatures, the input parameters incorporated in the

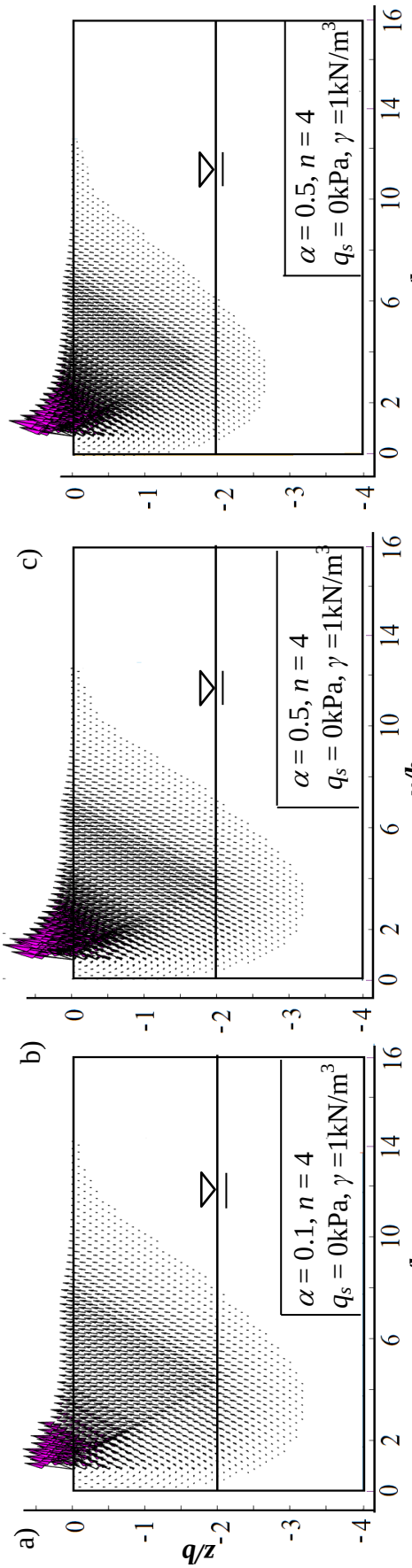

Figure 7.15 Nodal velocity pattern for strip footing on sandy soil (ϕ= 40°) for different α values: a) α = 0.1; b) α = 0.5; c) α =0.9.

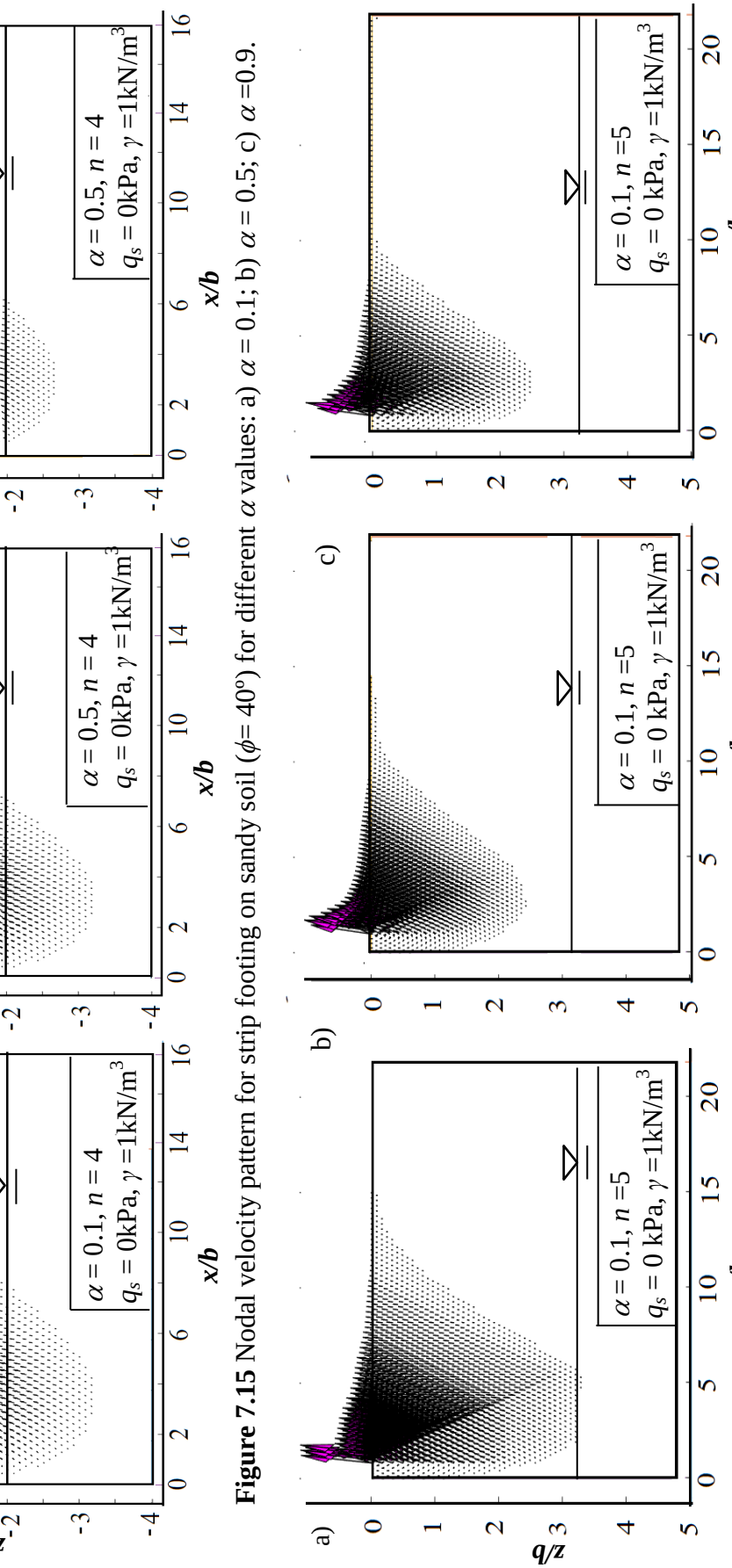

Figure 7.16 Nodal velocity pattern for strip footing on sandy soil (ϕ= 40°) for different K_M values: a) K_M = 0; b) K_M = 2; c) K_M=4.

Table 7.2 A comparison of q_u values for strip footing resting on unsaturated sandy soil

ϕ'	h_w	Present result[a]	Du.et al. (2021)[b]	Vahedifard and Robinson (2016)[c]
		q_u (kPa)		
35°x1.1*	0	279.50	466.49	312.24
	1	887.10	846.774	1330.91
	2	943.00	1071.43	1840
	4	697.00	867.512	1775.3
	6	650.80	812.212	1731.88
3°0x1.1*	0	104.64	141.379	101.5
	1	391.32	365.517	543.478
	2	379.50	448.276	768.116
	4	270.45	334.483	739.13
	6	248.27	313.793	717.4

Note: a: The solutions are obtained on the basis of FELA with the help of exterior point method.
b: The solutions are obtained on the basis of FELA with discretization techniques.
c: The solutions are obtained on the basis of effective stress approach with suction stress.
*: Increased 10% to incorporate the effect of dilation.

analysis are $\gamma = 18$ kN/m^3, $n = 4$, $\alpha = 0.1$kPa^{-1}, $k_s = 3\text{x}10^{-5}$ m/sec, $q = 1.15\text{x}10^{-8}$ m^3/sec, and $\phi = 33°$ and 38.5°. In this context, it is noteworthy that the friction angle referred here are the plane strain friction angle which is 10% higher than the triaxial friction angle. Although the trend of all the results is similar, nevertheless quite a notable deviation is observed between the present solutions and the solutions reported by Vahedifard and Robinson (2016). This can be attributed to the fact that unlike the continuous variation of matric suction adopted in the present work, Vahedifard and Robinson (2016) considered the average matric suction values for different depths. The present numerical solutions are comparable to some degree of satisfaction with the

analytical solutions provided by Du et al. (2021). It is noteworthy that this article does not incorporate the effect of net normal stress on the strength parameters.

7.4 LIMITATIONS

The numerical computations are performed by considering a wide number of assumptions. These idealizations are associated with the material properties, hydromechanical modelling, limit theorems, as well as solutions techniques. The flow characteristics and the strength parameters are idealized to be inherently homogenous, uniform, and stress (net-normal stress) independent. The flow is considered to be steady-state and unidirectional. The variation of saturation is considered to be solely dependent on the matric suction during a drained loading. The degree of saturation varies even for a constant matric suction and that is supposed to make an impact on the suction stress value. However, the present model is incapable of incorporating the effect of net normal stress induced volumetric deformation on the suction stress. The numerical simulations are carried out by considering the uniqueness of the soil retention curves. In reality, there exists an appreciable hysteresis between the drying and the wetting curves. The drying, wetting, and the scanning SWRC curves were reported (Tang et al., 2017; Yuan and Du, 2018, 2020; Fathipour et al., 2023) to manifest different load bearing capacity; the drying phase generates higher suction stress and eventually the maximum bearing capacity. The SWRC curves also get significantly influenced by the initial density and water content of the soil. The amount of hysteresis (area between the desorption and absorption SWRC) however, is relatively lesser for the highly-dense coarse-grained sands, especially, after multiple drying-wetting cycles. The assumption of isotropicity, perfect plasticity, associativity, coaxiality, linearization of yield criterion also impacts the computed solutions.

7.5 SUMMARY

By employing the upper bound limit analysis in conjunction with finite elements and linear optimization, this chapter presents the rigorous bearing capacity factors of strip footing rested on unsaturated sands. The unsaturated property of the stratum and the fluid flow of the soil are assumed to be governed by van-Genuchten's SWRC model and Gardner's permeability model, respectively. Instead of using matric suction, employment of suction stress in the formulation makes the analysis more flexible and the solutions more consistent and reliable. The numerical solutions are obtained by fluctuating the water table level and by duly incorporating the surcharging effect above the ground surface. The bearing capacity factors are greater for partially saturated soil as compared to fully saturated one. There is a certain water table position, referred here as critical water table, at which the computed bearing capacity is found to be maximum. This critical water table depth depends highly on the van-Genuchten model parameters, the strength of the soil as well as the soil-footing roughness condition. For the chosen soil which are having low air entry value, the bearing capacity factors does not vary with respect to the saturated coefficient of permeability and different flow conditions. Nodal velocity patterns are drawn for few cases. The volume of the influence zone, the nature and the magnitude of the velocity vectors, especially near the footing edge, are used for comprehending and explaining the variation of load-carrying capacity behavior with respect to the hydromechanical properties. The present solutions are verified with the results available in literature.